

Performance Evaluation of Bionax SR PVCO Pipeline with Extended Bell Joints under Earthquake-Induced Ground Deformation

by

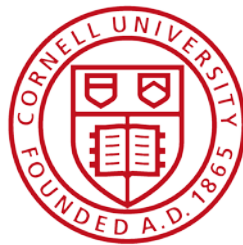
B. P. Wham

B. Berger

T. D. O'Rourke

C. Payiya-Ekkasut

H. E Stewart



Cornell University
School of Civil and Environmental Engineering
Cornell University
Hollister Hall
Ithaca, NY 14853
December, 2017

Acknowledgements

The authors wish to recognize the excellent effort of Cornell graduate and undergraduate students that made these experiments successful. Namely, the contributions of Christina Argyrou, Andrew Shakalis, Margaret Stack, George Howell III, Mia Stewart, Quinton Hubbell, Sarah Weinberg, Dara Karac, Corbin Akins, Maya Linden, and Charles Sanderson are gratefully acknowledged. Collaboration involving advanced instrumentation with colleagues at University of California Berkeley and the Center for Smart Infrastructure at Cambridge University is greatly appreciated. Support from the IPEX Group is gratefully acknowledged, as are the welcomed discussions with and contributions of Richard St. Aubin, Ryan Mintern, Trevor Johnston, and from IPEX.

Table of Contents

Acknowledgements	i
Table of Contents	ii
List of Figures	iv
List of Tables	vi
Section 1 Introduction	1
1.1. Report Organization	1
1.2. Previous Testing Program	1
1.3. Material Characterization	2
1.4. Joint Restraints	3
Section 2 Axial Tension Tests	5
2.1. Tension Test Setup	5
2.2. Instrumentation	5
2.3. Test Sequence	6
2.4. Experimental Results	7
2.4.1. Tension Test 1 (TT1) Results	7
2.4.2. Tension Test 2 (TT2) Results	9
2.4.3. Pipe Strains	11
2.5. Tension Test Comparison	11
2.6. Tension Test Summary	13
Section 3 Axial Compression Test	14
3.1. Introduction	14
3.2. Instrumentation	14
3.3. Test Sequence	16
3.4. Experimental Results	16
3.5. Compression Test Conclusions	19
Section 4 Four-Point Bending Test	20
4.1. Introduction	20
4.2. Setup and Instrumentation	20
4.3. Test Sequence	22
4.4. Experimental Results	24
4.4.1. Applied Vertical Displacement and Actuator Load	24
4.4.2. Bending Test Strains	25
4.4.3. Restrained Joint Moment-Rotation	26
4.4.4. Specimen Deflection	28
4.5. Four-Point Bending Test Conclusions	30
Section 5 Axial Pull Tests	32
5.1. Test Layout and Instrumentation	32

5.2.	Soil Placement and Compaction	34
5.2.1.	Axial Pull Test 1 (PT45): 45 in. Burial	35
5.2.2.	Axial Pull Test 2 (PT30): 30 in. Burial	36
5.2.3.	Axial Pull Test 3 (PT45b): 45 in. Burial, 1309 Restraint	36
5.2.4.	Axial Pull Test 4 (PT60): 60 in. Burial	37
5.3.	Axial Pull Forces and Displacements	37
5.3.1.	Interpretation of Measurements	38
5.3.3	Axial Pull Test 2 (PT30): 30 in. (70 mm) Burial Results	42
5.3.4	Axial Pull Test 3 (PT45b): 45 in. Burial 1309 Restraint Results	43
5.3.5	Axial Pull Test 4 (PT60): 60 in. Burial Results	45
5.4.	Comparison of Axial Load vs Displacement Performance	46
5.5.	Axial Pull Tests Summary	48
Section 6	Fault Rupture Simulation	49
6.1.	Experimental Setup	49
6.1.1.	Test Procedure	50
6.1.2.	Instrumentation	51
6.1.3.	Soil Preparation and Compaction Data	55
6.2.	Split Basin Test Results	57
6.2.1.	Test Basin Movements	57
6.2.2.	Internal Water Pressure	58
6.2.3.	End Loads	59
6.2.4.	Joint Opening	59
6.2.5.	Axial Strain and Force Distribution	60
6.2.6.	Bending Strain and Moment Distribution	62
6.3.	Post-test Photos	64
6.4.	Summary of Split Basin Test	64
Section 7	Summary	68
7.1.	Tension Test Summary	68
7.2.	Compression Test Summary	68
7.3.	Four-point Bending Test Summary	69
7.4.	Axial Pull Tests Summary	69
7.5.	Summary of Large-Scale Fault Rupture Effects	70
7.6.	Significance of Test Results	71
References		73

List of Figures

<u>Title</u>	<u>Page</u>
Figure 1.1. Longitudinal stress-strain results from Bionax tensile coupon specimens (Wham et al., 2017)	3
Figure 1.2. Circumferential elastic modulus variation from internal pressurization (Wham et al., 2017)	3
Figure 1.3. Two styles of tested joint restraints: (a) red 1559 and (b) black 1309 restraints, both produced by Ford Meter Box.	4
Figure 2.1. Plan view of tension test setup (TT2 with 1309 restraints shown)	5
Figure 2.2. Detailed view of joint configuration for (a) TT1 (1559 Restraints) and (b) TT2 (1309 Restraints) at the start of each test	6
Figure 2.3. TT1 actuator load vs. displacement	8
Figure 2.4. Axial load vs. joint displacement for TT1 and unrestrained joint	8
Figure 2.5. TT1 Test (a) just prior to failure and (b) after failure	8
Figure 2.6. TT2 actuator load vs. displacement	9
Figure 2.7. Axial load vs. joint displacement for TT2 and unrestrained joint	9
Figure 2.8. Successive images of TT2	10
Figure 2.9. TT1 bell and spigot strains	11
Figure 2.10. TT2 bell and spigot strains	11
Figure 2.11. Comparison of tension tests TT1, TT2, and TT3 and unrestrained pullout	12
Figure 3.1. Plan view of compression test specimen	15
Figure 3.2. Composite of (a) plan view and (b) photo of compression test joint initial condition	17
Figure 3.3. Axial compressive load vs. joint displacement for compression test	18
Figure 3.4. Pipe strains at north (bell) and south (spigot) gage planes	18
Figure 3.5. Post-test images of (a) joint profile and (b) cross-section cut of pipe showing wrinkling of spigot	18
Figure 4.1. Bending test specimen showing string potentiometer locations	21
Figure 4.2. Profile view of four-point bending test	21
Figure 4.3. Support saddle and roller for bending tests	22
Figure 4.4. Vertical displacement at loading points vs. time	25
Figure 4.5. Actuator load vs. time	25
Figure 4.6. Vertical displacements along the pipe specimen for various vertical load point displacements	25
Figure 4.7. Axial and circumferential strains at the crown and invert for planes SG+63 and SG-63	26
Figure 4.8. Axial strains at the specimen crown, invert, and springlines for planes SG+23 and SG-23	26
Figure 4.9. Crown strain at various levels of loading point vertical displacement	27

Figure 4.10.	Invert strain at various levels of loading point vertical displacement	27
Figure 4.11.	Applied moment vs. specimen deflection	28
Figure 4.12.	Restrained joint at several levels of imposed bending deformation	29
Figure 4.13.	Restrained joint bending test failure	30
Figure 4.14.	Failure of specimen at both the north and south restraints	30
Figure 5.1	Plan view of pull through specimen including approximate locations of nuclear densitometer and moisture content measurements	33
Figure 5.2.	Particle size distribution of RMS graded sand	35
Figure 5.3.	Ratio of axial secant modulus to elastic modulus vs. axial strain	39
Figure 5.4.	PT45 axial load vs. displacement plot for actuator, load cell, and strain gage loads 41	
Figure 5.5.	Soil surface cracking adjacent to north wall for PT45	41
Figure 5.6.	Photo of sand lodged between nuts and collar of the joint restraint	41
Figure 5.7.	PT30 axial load vs. displacement plot for actuator, load cell, and strain gage loads 42	
Figure 5.8.	Soil surface cracking for PT30	43
Figure 5.9.	PT45b axial load vs. displacement plot for actuator, load cell, and strain gage loads 44	
Figure 5.10.	Joint opening post PT45b	44
Figure 5.11.	PT60 axial load vs. displacement plot for actuator, load cell, and strain gage loads 45	
Figure 5.12.	Comparison of axial load vs displacement measurements	47
Figure 5.13.	Axial load vs. depth to centerline of pipe	48
Figure 6.1.	Plan view of split basin prior to fault rupture test	50
Figure 6.2.	Joint instrumentation (a) before and (b) after installation of joint shield	55
Figure 6.3.	Plan view of locations for compaction measurements	56
Figure 6.4.	Actuator Displacement vs. Time	58
Figure 6.5.	Actuator Force vs. Time	58
Figure 6.6.	Internal water pressure vs. fault displacement	59
Figure 6.7.	Measured north and south end force	59
Figure 6.8.	Initial conditions of restrained joint	60
Figure 6.9.	Joint opening displacement for both joints relative to fault displacement	60
Figure 6.10.	Evolution of average axial strains along pipeline at various magnitudes of fault movement	61
Figure 6.11.	Evolution of average axial force along pipeline at various magnitudes of fault movement	62
Figure 6.12.	Evolution of bending strains along the specimen at various levels of fault rupture	63
Figure 6.13.	Evolution of bending moment along pipeline at various magnitudes of fault movement	64

Figure 6.14. Overhead view of the (a) pipeline and (b) failed joint after excavation of the split basin test	65
Figure 6.15. View looking north of (a) failed pipeline and (b) close up of joint	66

List of Tables

<u>Title</u>	<u>Page</u>
Table 1.1. Comparison of PVCO anisotropic material properties (Wham et al., 2017)	3
Table 2.1. Instrumentation list for IPEX tension and compression tests	7
Table 3.1. Instrumentation for compression test	15
Table 4.1. Instrumentation for Bionax SR four-point bending test	23
Table 5.1. Instrumentation for IPEX pull-through tests	34
Table 5.2. PT45 Compaction Data	36
Table 5.3. PT30 Compaction Data	36
Table 5.4. PT45b Compaction Data	37
Table 5.5. PT60 Compaction Data	38
Table 6.1. IPEX split basin strain gage instrumentation list	52
Table 6.2. Instrumentation for IPEX split basin test	54
Table 6.3. Displacement instruments for IPEX split basin test	55
Table 6.4. Dry unit weights for IPEX pressurized pipe test	56
Table 6.5. Moisture tin water content data for IPEX pressurized pipe test	57

Section 1

Introduction

This report is submitted to the IPEX Group (herein referred to as IPEX). It presents results from a testing program to investigate the performance of 6-in. (150-mm)-diameter oriented polyvinyl chloride pipeline (commercially referred to as Bionax SR) with elongated bell-and-spigot restrained joints. The purpose of the testing is to evaluate the ability of the pipeline to accommodate axial and bending deformation and assess how pipelines composed of Bionax SR pipe with extended bell-and-spigot restrained joints respond to fault rupture, which not only represents surface faulting but also the most severe ground deformation that occurs along the margins of liquefaction-induced lateral spreads and landslides. The work was undertaken in the Cornell Large-Scale Lifelines Testing Facility, which is part of the Bovay Laboratory Complex at Cornell University.

1.1. Report Organization

The report is organized into seven sections. Section 1 provides introductory remarks and discusses previous testing. Section 2 and 3 provide the results of direct axial tension and compression tests, respectively. A four-point bending test is discussed in Section 4. Section 5 describes the test setup and results for axial pull-through tests performed on restrained joints in soil, and Section 6 reports on a large-scale split basin fault rupture test. Finally, Section 7 summarizes key findings from the preceding sections and provides general conclusions derived from the testing.

1.2. Previous Testing Program

The testing program is the second one performed at Cornell University on IPEX Bionax PVCO pipe. The initial series of tests, first reported by Stewart et al., (2013a, 2013b, and 2013c), took place in 2013 and included material characterization, axial tension and compression testing of the joints, four-point bending, and a fault rupture simulation of standard Bionax PVCO pipe. Based on recommendations from those tests, changes to both the bell and restraints were made to provide improved performance under large ground deformations. The outcome is the Bionax SR pipe, which has an extended bell, but the same material properties and barrel geometry as the Bionax product previously tested.

References to the first series of reports, available on the Geotechnical Lifelines Large-Scale Testing Facility website¹, and subsequent publications [i.e., Wham et al. (2017)], are made periodically throughout this report. Discussion of fundamental material characterization previously performed is provided in the following section for completeness.

1.3. Material Characterization

Unlike typical polyvinyl chloride (PVC) pipe, the manufacturing process for oriented polyvinyl chloride (PVCO) pipe results in a biaxial molecular structure. During the forming process, expansion of the pipe aligns the polymer chains circumferentially, and extrusion provides orientation in the axial direction. The net result is a transversely anisotropic material with different strength and stiffness characteristics in the axial and circumferential directions of the pipe wall.

Material characteristics of Bionax pipe were reported in previous publications prepared by researchers at Cornell University. Stewart et al. (2013a) provides detailed results for 11 tensile coupon tests performed on specimens cut longitudinally from 6-in. (150-mm) and 8-in. (200-mm)-diameter pipe walls. Wham (2016) discusses a procedure for determining circumferential properties from strain gage data recorded during a high internal pressure test. Select results from material characterization performed by Wham et al., (2017) are summarized in Table 1.1.

Figure 1.1 shows representative engineering stress versus strain curves from select tensile coupon tests performed at an ambient temperature of 72°F (22°C) and strain rates of approximately 25 to 35 %/min. Estimates of longitudinal elastic modulus, 450 ksi (3.10 GPa), and Poisson's ratio, 0.37, were determined from the linear portion of the coupon test results.

As explained by Wham et al., (2017), to evaluate circumferential properties, an 8-ft (2.4-m)-long section of 6-in. (150-mm)-diameter pipe was instrumented with strain gages, fitted with end caps and pressurized with water to a maximum internal pressure of 400 psi (2.76 MPa), imposing stress levels exceeding the elastic range of the material. Figure 1.2 shows the circumferential modulus plotted relative to the internal pipe pressure. A circumferential elastic modulus, $E_{\theta} = 538$ ksi (3.71 GPa), fits the data in the linear elastic range of response, after which the apparent modulus decreases with increasing pressure due to plastic deformation.

¹ <https://lifelines.cce.cornell.edu/>

Table 1.1. Comparison of PVCO anisotropic material properties (Wham et al., 2017)

PVCO Material Properties	Young's Modulus [GPa(ksi)]	Poisson's Ratio	Proportional Limit [MPa (ksi)]	Proportional Limit Strain	Average Maximum Stress [MPa (ksi)]	Average Strain at Maximum Stress
Longitudinal	3.10 (450)	0.37	24.8 (3.6)	0.008	57.5 (8.34)	0.0502
Circumferential	3.71 (538)	0.44	NA	NA	NA	NA

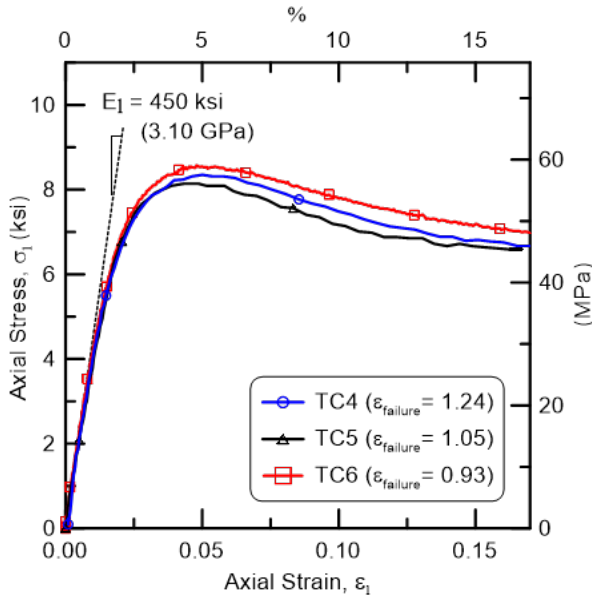


Figure 1.1. Longitudinal stress-strain results from Bionax tensile coupon specimens (Wham et al., 2017)

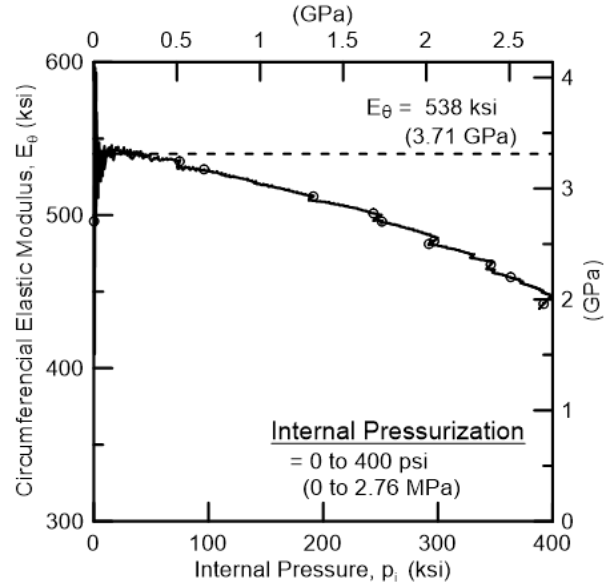


Figure 1.2. Circumferential elastic modulus variation from internal pressurization (Wham et al., 2017)

1.4. Joint Restraints

Two different joint restraints were investigated to determine which device is best suited for (1) providing axial restraint to joint pullout, therefore developing strain along the pipeline after joint engagement, and (2) promoting relative movement between pipeline and soil during large deformation. The objectives were achieved during the direct tension and axial pull through tests, respectively, as reported herein.

Figure 1.3 provides a comparison of the two joint restraints used in testing. Both are commercially available Uni-Flange® Pipe Restraints for AWWA C909 Pipe and manufactured by The Ford Meter Box Company, Inc. in Wabash, Indiana.

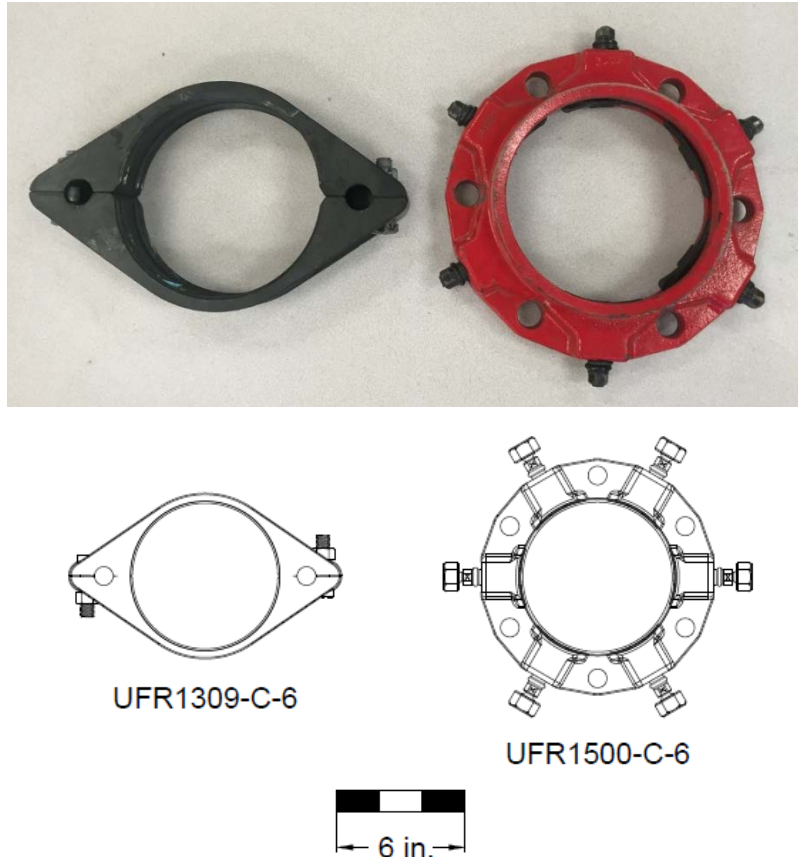


Figure 1.3. Two styles of tested joint restraints: (a) red 1559 and (b) black 1309 restraints, both produced by Ford Meter Box.

The red Series 1559 Restrainer consists of two Series 1559 “Circle Lock” (UFR1500-C-6-U) style restraints, hereafter referred to as “1559 restraints”, constructed of ASTM A536 ductile iron (Grade 65-54-12). The design incorporates a series of six individually torqued iron segments (with twist off torque heads), spaced circumferentially around the pipe, which distribute the restraining force to the pipe body. Restraints on either side of the joint are linked by six 5/8 in. (15.8 mm) threaded steel rods and nuts.

The black 1399 Restrainer consists of two UFR1309-C-6 style split restraints, hereafter referred to as “1309 restraints”, which are constructed of ASTM A536 ductile iron (Grade 65-54-12) or ASTM A36 structural steel. The restraints on either side of the joint are connected by two 3/4 in. (19 mm) threaded steel rods and nuts. Positive connection to the pipe body is provided by four continuous serrations on the inside of each half of the restraint. When the two clamping bolts are tightened, the serrations penetrate the outer circumference of the pipe barrel.

Section 2

Axial Tension Tests

Two tension tests, TT1 and TT2, were performed on IPEX joints using two different joint restraints. The testing was performed to characterize the axial force vs displacement performance of the joints and to compare their behavior with respect to axial force and strain along the pipeline during ground movement.

2.1. Tension Test Setup

Figure 2.1 is a plan view of the tension test setup for both tests. The 22 kip (98 kN), 10 in. (250 mm) stroke actuator and load cell were positioned at the south end of the specimen. Load was applied by the actuator through 5/8 in. rods and nuts connected to three 1559 restraining collars to provide adequate grip. A similar assembly of restraining collars gripped the north end of the specimen. Figures 2.2 a) and b) are plan views of the joints and restraints for tension tests TTI and TT2, respectively. Precise dimensions are shown for the locations of the 1559 and 1309 restraints as well as the initial settings of the nuts on the threaded rods.

2.2. Instrumentation

The instrumentation listed in Table 2.1 was identical for each tension test. At the south end of the setup, actuator displacement was recorded internally, and axial load was provided by the load cell. Internal pressure was recorded at the north end by a pressure transducer.

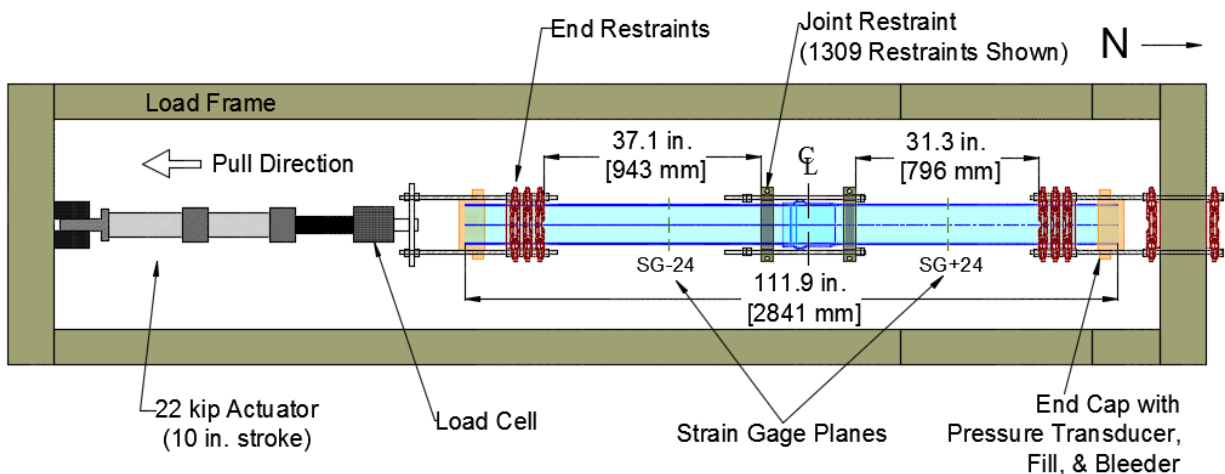


Figure 2.1. Plan view of tension test setup (TT2 with 1309 restraints shown)

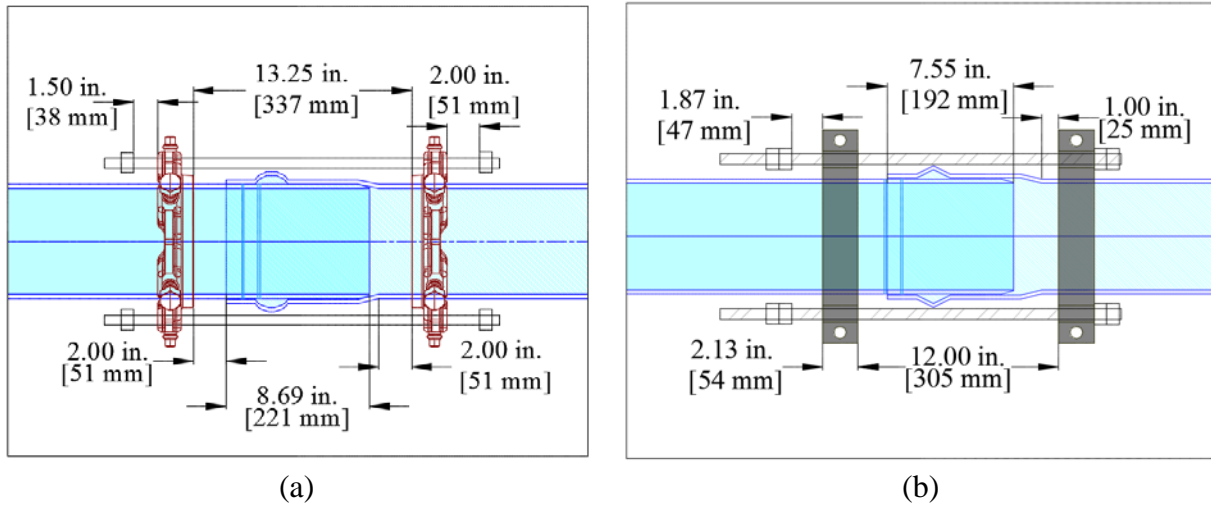


Figure 2.2. Detailed view of joint configuration for (a) TT1 (1559 Restraints) and (b) TT2 (1309 Restraints) at the start of each test

A total of 12 strain gages were instrumented to measure localized specimen deformation. Gage planes were located 24 in. (610 mm) to the north and south of the specimen centerline. Strain gage plane SG+24, located on the north (bell) section of pipe, consisted of four axial gages placed circumferentially around the specimen at the crown, invert, and east and west springlines. Plane SG-24 included four axial and four circumferential gages, one of each at the crown, invert, and east and west springlines. String potentiometers (string pots) were set at various locations along the specimen to record displacements.

2.3. Test Sequence

After the test specimen was centered in the frame and all instrumentation installed, the test commenced by starting the data acquisition system at a rate of 2 Hz. Nuts on the threaded rods at either end of the specimen were tightened to limit movement of the system during pressurization. Tightening the nuts also serves to ensure the axial force imposed by pressurization is recorded by the load cell. Once pressurized to approximately 80 psi (550 kPa), an actuator stroke of 10 in. (250 mm) was applied at a rate of 1 in./min (25 mm/min). The tests continued until rupture or pullout with an accompanying inability to hold pressure.

Table 2.1. Instrumentation list for IPEX tension and compression tests

Location	Instrument Description	Local Instrument Name
24 in. (610 mm) North of Centerline	East, Axial Strain	SG+24EA
	Crown, Axial Strain	SG+24CA
	West, Axial Strain	SG+24WA
	Invert, Axial Strain	SG+24IA
24 in. (610 mm) South of Centerline	East, Axial Strain	SG-24EA
	Crown, Axial Strain	SG-24CA
	West, Axial Strain	SG-24WA
	Invert, Axial Strain	SG-24IA
	East, Circumferential	SG-24EC
	Crown, Circumferential	SG-24CC
	West, Circumferential	SG-24WC
	Invert, Circumferential	SG-24IC
S End to Bell	Horizontal String Pot	HSP_S_BELL
S End to S Restraint	Horizontal String Pot	HSP_S_S-REST
S Restraint to N Restraint	Horizontal String Pot	HSP_S-REST_N-REST
N Restraint to N End	Horizontal String Pot	HSP_N-REST_N
South of Load Frame	Actuator Displacement	22Kip_Displacement
South of Load Frame	Actuator Load	55Kip_Load
North End Cap	Pressure Sensor	Pressure

2.4. Experimental Results

The following subsections provide results from the two tension tests.

2.4.1. Tension Test 1 (TT1) Results

Actuator force versus displacement for the first tension test, TT1, with red 1500 restraints is provided in Figure 2.3. There was an increase in displacement under negligible load until 3.5 in. (89 mm) when the joint restraints were engaged, generating axial force. The actuator load increased at a relatively constant rate with actuator displacement.

Figure 2.4 shows axial load versus joint displacement for TT1 as well as a preliminary pullout test on an unrestrained joint. The joint displacement refers to the relative movement between the bell and spigot. The unrestrained pullout test demonstrates that from a fully inserted position, the joint

has 5.75 in. (146 mm) of axial displacement capacity before the end of the spigot disengages with the gasket, which leads to leakage at the joint.

At an axial load of 21.8 kips (97 kN) and a joint opening of 4.9 in. (124 mm), the specimen ruptured at the bell side (north) restraint. Figure 2.5 presents photos of the TT1 specimen just before and after failure. Post-test assessment indicates that a circumferential fracture propagated from the indentations of the restraint teeth. No leakage of the specimen was observed prior to rupture.

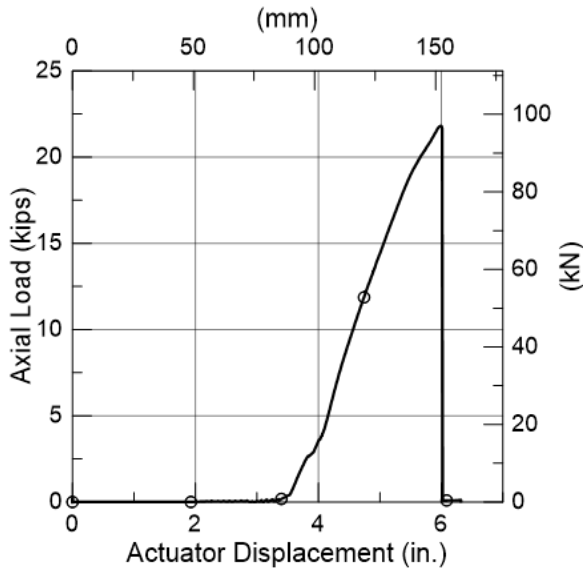


Figure 2.3. TT1 actuator load vs. displacement

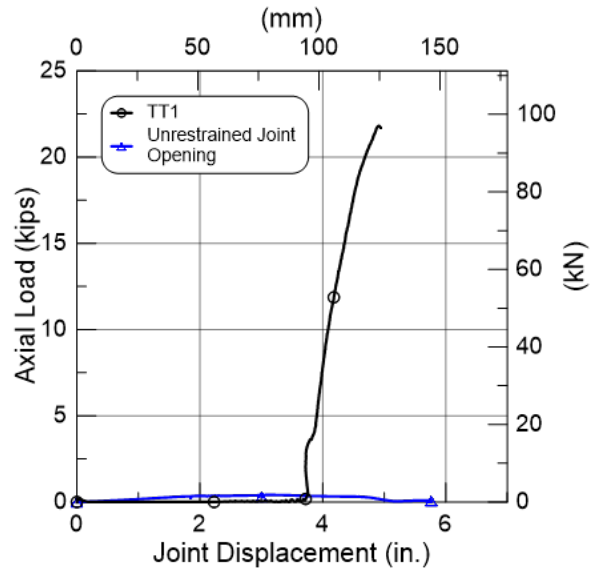


Figure 2.4. Axial load vs. joint displacement for TT1 and unrestrained joint

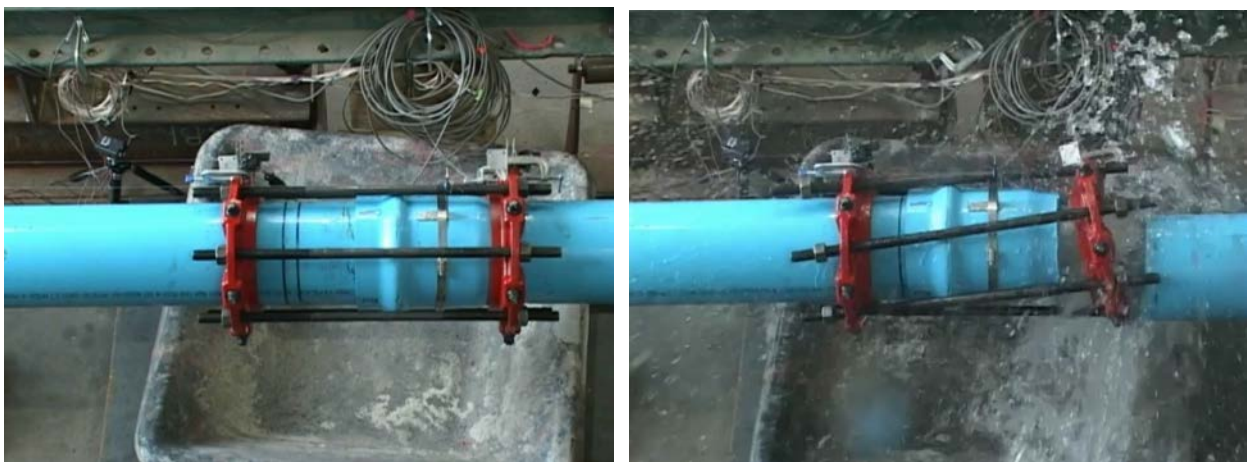


Figure 2.5. TT1 Test (a) just prior to failure and (b) after failure

2.4.2. Tension Test 2 (TT2) Results

The second tension test (TT2) was performed with black 1309 restraints. Figure 2.6 shows the axial load versus actuator displacement for TT2. As shown in Figure 2.2(b), the restraining nuts for this specimen were set at 1.87 in. (47.5 mm). There is negligible load in the specimen until 1.87 in. (47.5 mm), after which the load increases rapidly.

Figure 2.7 provides the axial load versus joint opening for TT2 and an unrestrained joint (as described in the previous section). At a load of 12.7 kips (56.5 kN) and actuator displacement of 3.1 in. (79 mm) in Figure 2.6, slippage between the pipe and restraint occurred, accompanied by a drop in axial load. The joint displacement was 2.3 in. (58 mm), as shown in Figure 2.7. Slippage and ratcheting continued with additional axial displacement. The six peaks in loading, shown in Figure 2.6 and Figure 2.7, correspond to individual slippage events. After each slip, the restraint reengaged with the pipe wall and loading increased. The maximum axial load achieved during the test was 14.7 kips (65.4 kN). No leakage was observed until the last slippage event, corresponding to a joint opening of 5.75 in. (146 mm).

Figure 2.8 provides a series of images captured from video of the tension test. Figure 2.8 (b) shows an image of the specimen just before the first load drop, where rotation of the restraints is evident. This rotation promoted slippage at the interface between the pipe and restraint. While indentations

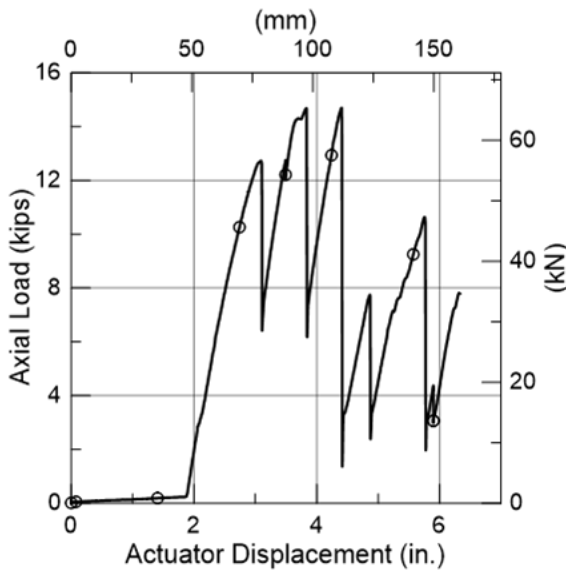


Figure 2.6. TT2 actuator load vs. displacement

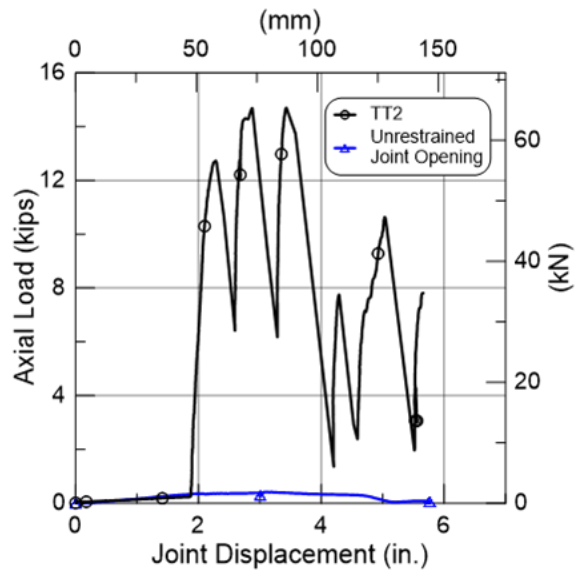
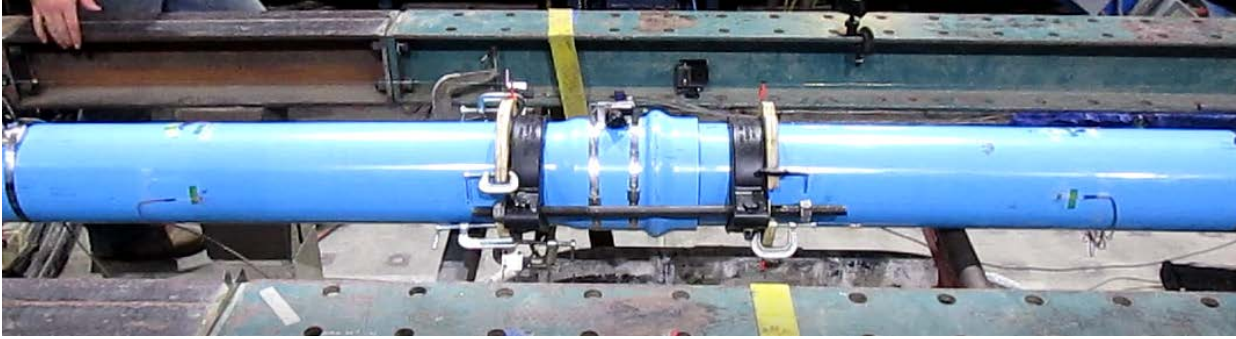
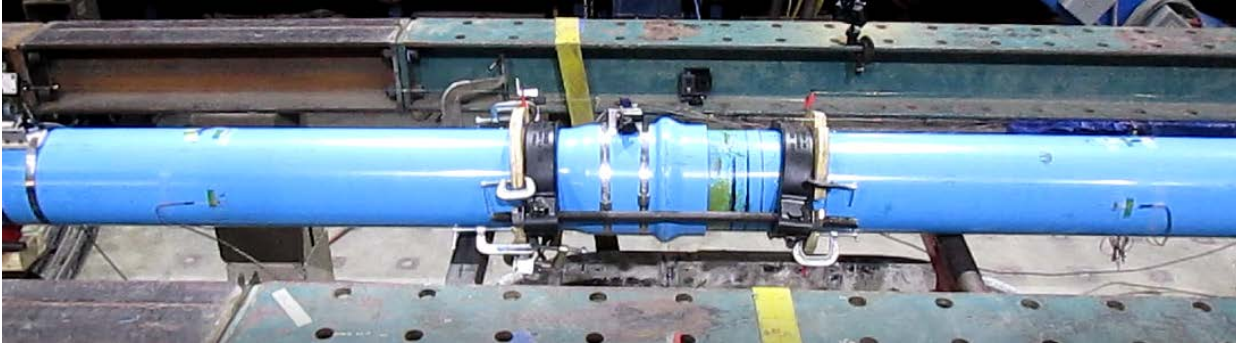


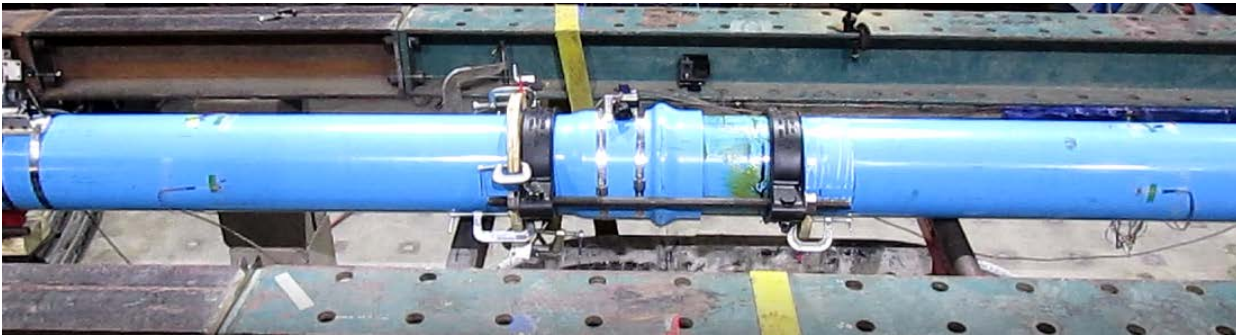
Figure 2.7. Axial load vs. joint displacement for TT2 and unrestrained joint



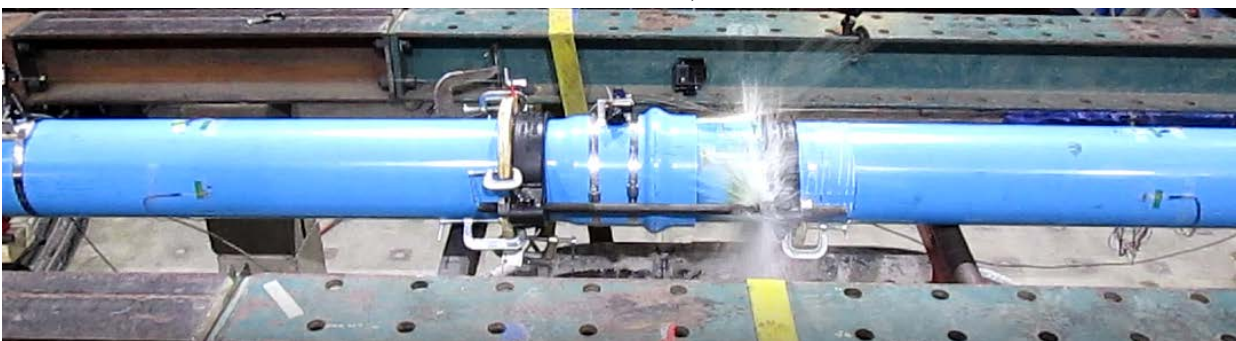
(a) Start of TT2 test (note nuts provide approx. 1.8 in. (47 mm) of pullout)



(b) Just before first ratcheting event (note bending of black restraints)



(c) After several ratcheting events, just before leakage (note scarring of pipe on the right side of the south restraint)



(d) Leakage of joint

Figure 2.8. Successive images of TT2

of the pipe wall were visible on the right side of the south restraint, as shown in Figure 2.8(c), neither leakage nor rupture occurred until the last increment of slippage.

2.4.3. Pipe Strains

Strains were recorded at two planes along the specimen, as shown in Figure 2.1. Figure 2.9 and Figure 2.10 provide average bell and spigot axial strains versus joint displacement for TT1 and TT2, respectively. The figures also include circumferential strains averaged from four strain gages spaced evenly around the pipe. Initial increases in circumferential strain, due to internal pipe pressurization, are accompanied by negative (compressive) axial strains resulting from Poisson's effect. Engagement of the joint restraints is denoted by a sharp increase in axial strain with additional joint displacement. TT1 reached a maximum average axial strain of 0.0093 (0.93%) while TT2 reached a maximum value of 0.0053 (0.053%). The comparison shows that TT1, with red 1559 restraints at the joint, achieved 40% greater strain than TT2, joined with black 1309 restraints. TT2 reached a total joint displacement of 5.9 in. (150 mm) prior to leakage, which has the potential to exceed the joint displacement of TT1, depending on where the restraining nuts are set during installation.

2.5. Tension Test Comparison

Comparisons between the two pressurized tension tests are shown in Figure 2.11. The figure also includes results from an unrestrained joint opening test and an unpressurized axial pull test (TT3) with red 1559 restraints. The unpressurized test was performed to show the axial performance of the pipe without internal water pressure. The results from the unrestrained test show the maximum

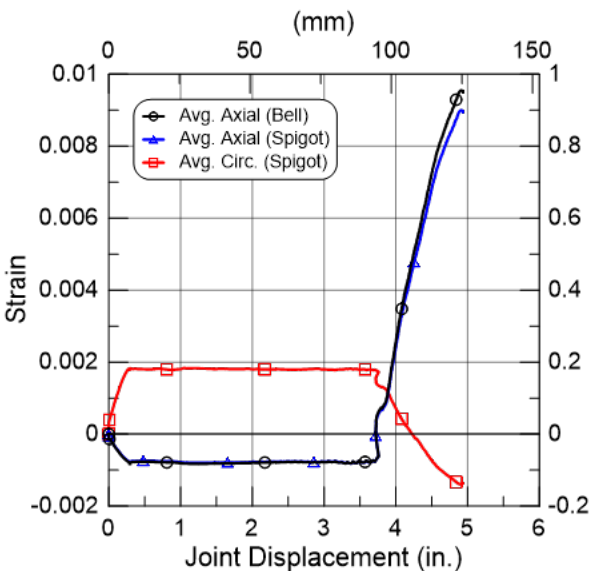


Figure 2.9. TT1 bell and spigot strains

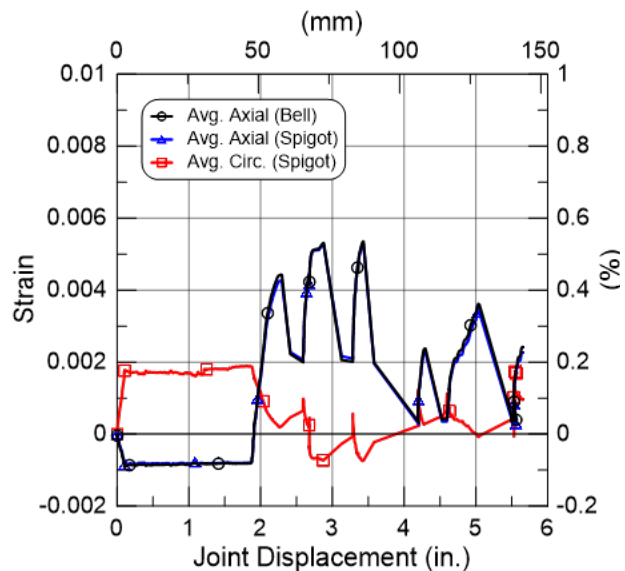


Figure 2.10. TT2 bell and spigot strains

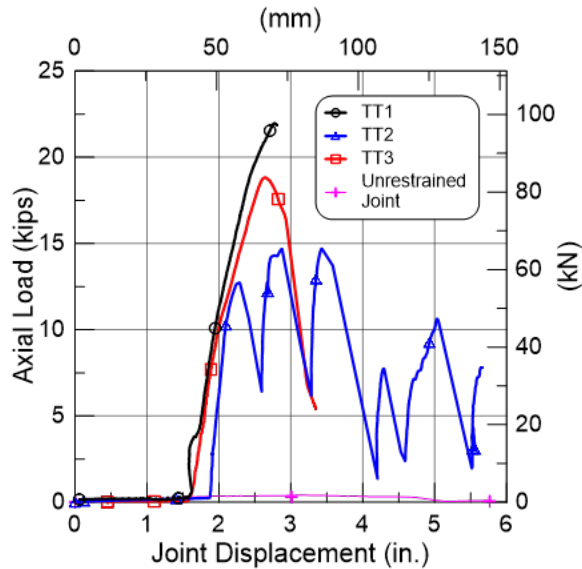


Figure 2.11. Comparison of tension tests TT1, TT2, and TT3 and unrestrained pullout

axial displacement capacity from a fully inserted position. Without a joint restraint, the previously tested Bionax joint had 3.9 in. (99 mm) of available axial displacement before leakage from pullout. Testing of the Bionax SR without joint restraint demonstrated that the joint has a maximum stroke of 5.9 in. (150 mm) before leakage from a fully inserted position.

The allowable joint displacement is a function of the initial joint insertion and where the restraining nuts are set. All tests started from a fully inserted position, but TT1 and TT2 had different allowable displacements. For Figure 2.11, the joint displacement from TT2 was adjusted to assume 2 in. (50 mm) of allowable pullout, providing comparable data between tests. These test results show that the red 1559 restraints for a pressurized pipe provide 40% more load capacity compared to the black 1309 restraints and thus are able to mobilize approximately 40% more axial elongation in the pipe compared to the elongation that accompanies the maximum load before slippage with the black 1309 restraints. However, the slippage associated with the 1309 restraints results in greater axial displacement of the joint relative to that attained with the 1559 restraints.

There is a trade-off in the amount of ground deformation that can be accommodated by each restraint. The 1559 restraints result in more elongation, or stretch, in the pipe between joints, whereas the 1309 restraints result in more slip at the individual joints with less pipe elongation. If the 1309 restraints could be improved to hold load comparable to the load capacity of the 1559 restraints, they would provide a more effective restraining device. Their smaller size and lower

number of rods make them more attractive for ease of field installation. Moreover, they would provide less resistance to pulling through the soil during ground deformation, thus allowing for more ground movement before failure. Axial restraint against ground deformation is evaluated with respect to the two restraint types in Section 5.

2.6. Tension Test Summary

Two tension tests are reported using two different joint restraints. The intention of testing both restraints was to determine which was best suited for developing axial force and strain along the pipeline during ground movement. These test results show that the Ford Meter Box 1559 restraints for a pressurized pipe provide 40% more load capacity compared to the Ford Meter Box 1309 restraints, and thus are able to mobilize approximately 40% more axial elongation in the pipe compared to the elongation that accompanies the maximum load before slippage with the black 1309 restraints. However, the slippage associated with the 1309 restraints results in greater axial displacement of the joint relative to that attained with the 1559 restraints. The 1559 restraints result in more elongation, or stretch, in the pipe between joints, whereas the 1309 restraints result in more slip at the individual joints with less pipe elongation.

Section 3

Axial Compression Test

3.1. Introduction

This section summarizes the results of compression testing of the IPEX Bionax SR joint with joint restraints. The compression test is designed to demonstrate the joint's performance under axial load and internal water pressure representative of typical operating conditions.

The specimen consisted of two sections of PVCO pipe connected by a Bionax SR bell and spigot joint with 1559 restraints. As shown in Figure 3.1, the total specimen length was 124 in. (3.1 m). End caps were used at either end of the specimen to apply internal water pressure. A series of three 1559 restraints were used at either end of the specimen to transfer load from the actuator and loading frame to the specimen.

3.2. Instrumentation

The compression test setup and instrumentation, as shown in Figure 3.1, were nearly identical to those used in the tension tests (see Figure 2.1), with the only exception being that the overall specimen length was approximately 12 in. (300 mm) longer to accommodate the retracted initial position of the actuator. The actuator used for the compression test had a load capacity of 22 kips (98 kN) and stroke of 10 in. (250 mm). A list of instruments is provided in Table 3.1, which are described previously in Section 2.2 of this report.

A total of 12 strain gages were fixed to the exterior of the specimen on two designated planes: SG-24 and SG+24, as shown in Figure 3.1. For each plane, the gages were located at the crown, invert, and east and west springlines. Gage plane SG+24 was positioned on the bell section of the pipe 24 in. (610 mm) north of the specimen's center, as shown in Figure 3.1. This plane included four gages oriented in the axial direction. Plane SG-24 was positioned on the spigot section of pipe 24 in. (610 mm) south of the joint center. It included four gages oriented in both the axial and circumferential directions.

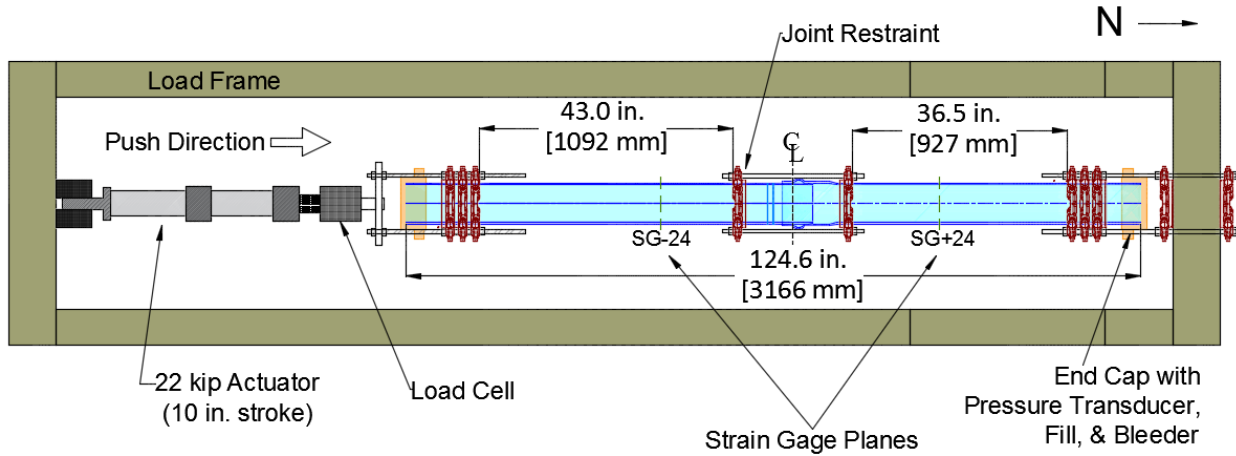


Figure 3.1. Plan view of compression test specimen

Table 3.1. Instrumentation for compression test

Location	Instrument Description	Local Instrument Name
24 in. (610 mm) North of CL	East, Axial Strain	SG+24EA
	Crown, Axial Strain	SG+24CA
	West, Axial Strain	SG+24WA
	Invert, Axial Strain	SG+24IA
24 in. (610 mm) South of CL	East, Axial Strain	SG-24EA
	Crown, Axial Strain	SG-24CA
	West, Axial Strain	SG-24WA
	Invert, Axial Strain	SG-24IA
	East, Circumferential	SG-24EC
	Crown, Circumferential	SG-24CC
	West, Circumferential	SG-24WC
Invert, Circumferential	SG-24IC	
S to Bell	Horizontal String Pot	HSP_S_BELL
S to S-Rest.	Horizontal String Pot	HSP_S_SRESTRAINT
S-Rest. to N Rest.	Horizontal String Pot	HSP_S-REST_N-REST
N-Rest to N	Horizontal String Pot	HSP_NRESTRAINT_N
South of Load Frame	22 Kip Displacement	22Kip_Dis
South of Load Frame	55 Kip Load	55Kip_Load
North End Cap	Pressure Sensor	Pressure

3.3. Test Sequence

After the specimen was instrumented and centered in the test frame, the test sequence began by starting the data acquisition system and laboratory hydraulic systems. The data sampling rate was 2 Hz. The north end restraining nuts were slowly tightened to bring the specimen in contact with the southern load cell/actuator. These adjustments ensured concentric initial loading conditions and restrained the pipe from axial movement due to internal pressure. Approximately 80 psi (550 kPa) of internal water pressure was applied. The measuring systems were checked, and an initial actuator displacement of 8 in. (200 mm) was applied.

The compression test was run to evaluate the axial compressive load versus displacement response of the joint, with particular attention to this relationship after the spigot made contact with the inside of the bell. Since no leakage or specimen damage was apparent after 8 in. (200 mm) of applied load, the actuator was retracted and three additional loading sequences were applied. While the additional loading did promote joint displacement, each of these loading sequences was stopped due to bending of the loading rods at the south end of the specimen.

3.4. Experimental Results

This subsection presents key experimental results including the compressive force versus displacement response of the restrained joint. During test setup, the spigot was fully inserted into the bell, the nuts on the joint restraints were set to allow 3.5 in. (90 mm) of joint opening, and internal pressure was introduced into the system allowing the joint to open and reach the initial test position shown in Figure 3.2. Loading from this initial position allowed for the measurement of compressive load before and after the spigot made contact with the back end of the bell.

Figure 3.3 shows several changes in axial response during the first loading sequence, identified by letters A through C in the figure. At 3.5 in. (90 mm) of joint closure (point A) the spigot makes contact with the inside of the bell. At approximately 4.6 in. (115 mm) (point B) the spigot reaches the collar of the bell restraint, requiring greater axial force to displace past this location. At 6.25 in. (160 mm) (point C) the spigot restraint makes contact with the bell face (refer to Figure 3.2(a)). At this point, the spigot begins to move relative to the spigot restraint, increasing the joint closure while the restraints remain at a constant spacing. Despite some minor striations on the spigot outer wall, significant damage to the pipe did not occur as a result of this relative displacement.

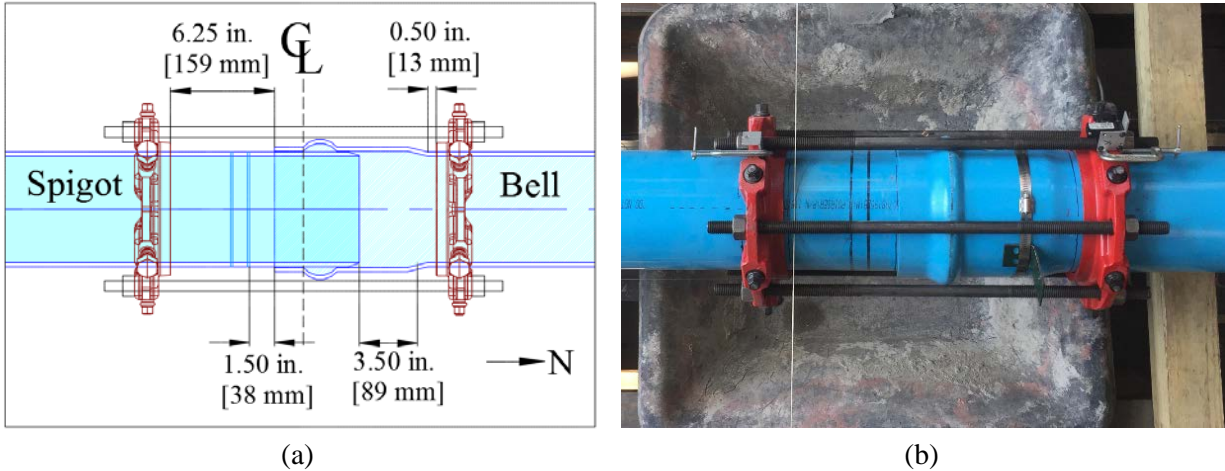


Figure 3.2. Composite of (a) plan view and (b) photo of compression test joint initial condition

The first 8 in. (200 mm) of imposed actuator displacement corresponded to a maximum joint displacement of 7.2 in. (183 mm) and a compressive load of 14.5 kips (64.5 kN). A maximum joint compressive load of 16.3 kips (72.5 kN) was briefly sustained at 9.7 in. (246 mm) of joint displacement during the fourth loading sequence.

Internal water pressure remained relatively constant at 80 ± 10 psi (550 ± 70 kPa) throughout the loading sequence. At no point during the compression test did the joint leak or rupture.

Strain gage measurements were used to provide a redundant measurement system for applied pipe force and to assess how joint response under large deformation is related to deformation of the adjacent pipe barrel. Axial and circumferential strain gage measurements located north (bell) and south (spigot) of the joint are presented in Figure 3.4. Each curve in the figure represents the average of four gages positioned circumferentially around the pipe. The north and south axial strains are virtually identical. Both the axial and circumferential strains show some strain at zero displacement. These initial strains of about $\epsilon_{axial} \approx -0.1\%$ and $\epsilon_{hoop} \approx 0.2\%$ are due to initial internal pressurization. The maximum applied load resulted in maximum axial and circumferential strains of -0.9% and 0.5% , respectively.

Figure 3.5 provides photos of the pipe specimen after testing. A comparison between Figure 3.2(b) and Figure 3.5(a) shows that the restraining collar on the bell side of the joint remained relatively stationary. Following the test, the bell was cut to provide the cross-sectional view of the joint in Figure 3.5(b). As the spigot was pushed under compressive load past the bell side collar, wrinkling around the pipe resulted in a reduction of the spigot diameter. This reduction in diameter allowed

the spigot to slip into the barrel of the adjoining pipe under modest levels of compressive load. This movement occurred without compromising the pressure seal provided by the gasket.

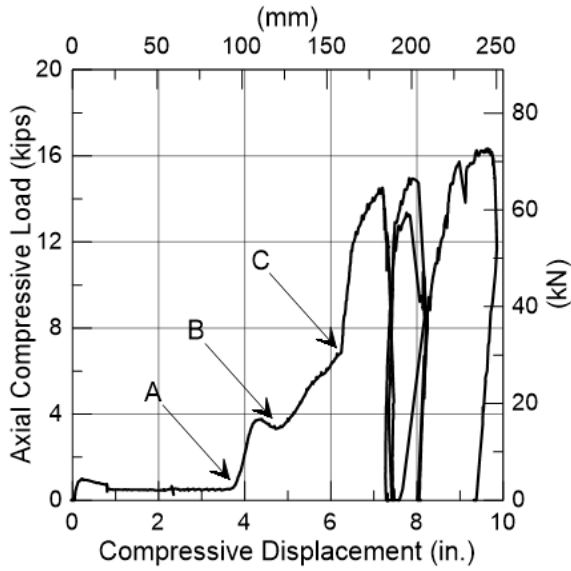


Figure 3.3. Axial compressive load vs. joint displacement for compression test

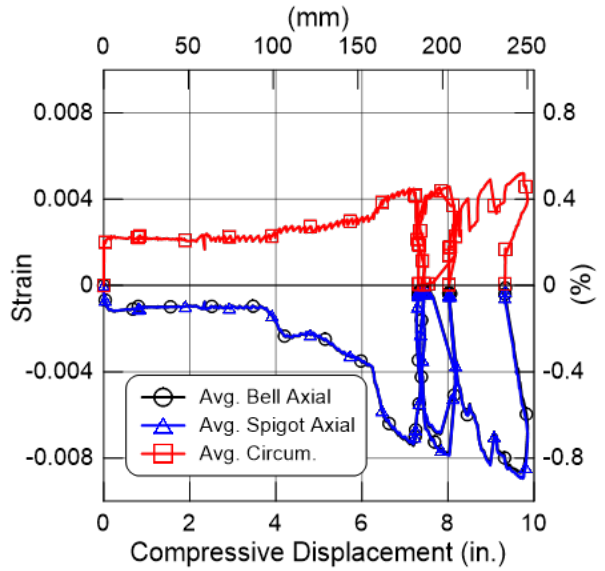
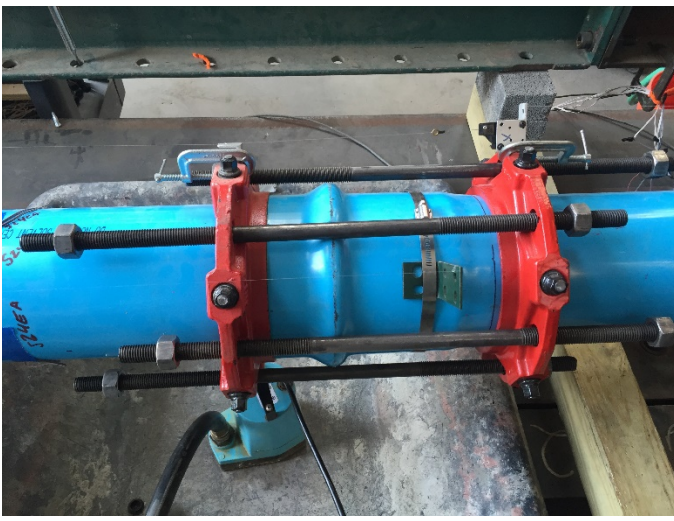


Figure 3.4. Pipe strains at north (bell) and south (spigot) gage planes



(a)



(b)

Figure 3.5. Post-test images of (a) joint profile and (b) cross-section cut of pipe showing wrinkling of spigot

3.5. Compression Test Conclusions

A compression test was performed on a 124 in. (3.1 m) long section Bionax SR pipe with the bell and spigot joint centered between two 1559 restraints. The pipe was pressurized with approximately 80 psi (550 kPa) of water throughout the test. An initial actuator displacement of 8 in. (200 mm) was applied to the pipe section, followed by several additional shorter loading sequences for a total 9.7 in. (296 mm) displacement at the joint. The joint sustained significant compressive deformation without leakage or loss of internal pressure. The spigot was pushed 6.5 in. (165 mm) and 5.1 in. (130 mm) past the end of the bell and bell collar location, respectively, demonstrating the capacity of the Bionax pipe with extended bell to accommodate axial compression. The compressive force versus axial displacement relationship for this test is consistent with the results of previous testing performed at Cornell University on Bionax bell and spigot joints (Stewart et al., 2013a).

In parallel with the Cornell tests, IPEX performed a high internal pressure test on an unrestrained 8 in. (200 mm) Bionax joint that had been over inserted 8 in. (200 mm) past the 6.7 in. (170 mm) suggested insertion line (Sanchez, 2013). Despite the spigot being pushed approximately one diameter past the fully inserted position, IPEX reports that the specimen complied with the minimum requirements for both long-term, 500 psi (3.45 MPa), and quick burst, 755 psi (5.21 MPa) pressures, in accordance with ASTM D1598 and D1599 standards, respectfully.

Section 4

Four-Point Bending Test

4.1. Introduction

This section summarizes the results of a four-point bending test on a restrained Bionax SR joint. Figure 4.1 shows a profile view of the test setup including dimensions of the test specimen. Caps were installed at each end of the specimen to allow for internal pressurization. The retaining nuts were set to allow 3 in. (75 mm) of joint opening from the fully inserted position. After internal pressure had opened the joint 3 in. (75 mm), vertical displacement was applied.

4.2. Setup and Instrumentation

Profile views of the test setup are shown in Figures 4.1 and 4.2. An MTS four-post load frame with a 200 kip (890 kN) capacity and 6 in. (152 mm) stroke was used for the test. Support and loading points were positioned 90 in. (2.29 m) and 30 in. (0.76 m), respectively, on either side of the center of the joint. Specially designed support saddles, shown in Figure 4.3, were used at each of the four contact points to distribute stress and prevent local deformation and ovaling of the specimen as well as provide an adequate surface for roller interaction.

Applied load and displacements were recorded throughout the test sequence. An electronic pressure transducer, located at the south end cap, measured internal water pressure. Four planes of strain gages were installed along the pipe. The gage planes are shown in Figure 4.1, and information about the individual gages is provided in Table 4.1.

Also shown in Figure 4.1 are the nine string potentiometers (string pots) used to measure vertical displacements along the specimen. String pots were fixed between the frame and the invert of the specimen at equal distances of 10, 30, 60, and 82 in. (250, 760, 1520, and 2080 mm) either side of the centerline of the test setup to measure vertical displacement. Each string pot location is labeled with respect to distance; e.g., VSP-30 was located at 30 in. (760 mm) to the right of the test centerline in Figure 4.1. Two additional string pots were attached at the crown and invert horizontally spanning the joint to provide a measure of joint rotation (or deflection). The instrument locations and names are listed in Table 4.1.

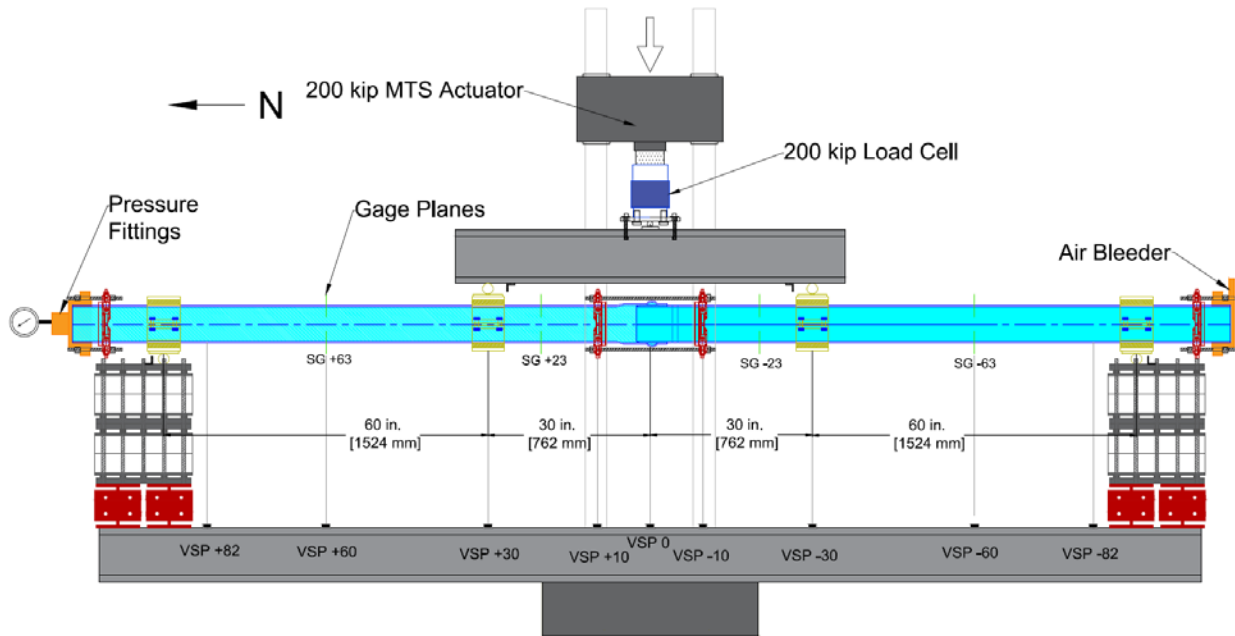


Figure 4.1. Bending test specimen showing string potentiometer locations



Figure 4.2. Profile view of four-point bending test



Figure 4.3. Support saddle and roller for bending tests

4.3. Test Sequence

After the specimen was instrumented, filled with water, and centered in the test frame, the test sequence was initiated by starting the data acquisition system and the hydraulic load frame. The data sampling rate was 2 Hz. The joint was slowly opened 3 in. (75 mm) under low levels of internal pressure. The specimen was then pressurized to approximately 80 psi (550 kPa) and manually adjusted during the test to be within ± 10 psi (70 kPa) of the initial value. Jacks supporting the center of the specimen were removed. The cross-head and actuator were lowered until the spreader beam came in contact with the loading points (rollers). Adjustments were made to the position of the spreader beam and rollers to ensure symmetric loading conditions.

Loading began by disengaging the locks and allowing the crosshead to move vertically downward. Crosshead displacement rate ranged from 1.75 to 2.5 in./min (44.5 to 63.5 mm/min). Loading was paused at approximately 14 in. (355 mm) of crosshead displacement to allow surveying of the specimen springline. Crosshead displacement continued until 18 in. (457 mm) of vertical displacement, at which time the crosshead was locked and loading was continued under servo control using the 6 in. (152 mm) stroke MTS actuator at a rate of 1 in./min (25.5 mm/min).

Table 4.1. Instrumentation for Bionax SR four-point bending test

Location	Instrument Description	Local Instrument Name
63 in. (1600 mm) North of CL	Crown, Axial Strain	SG+63CA
	Crown, Circumferential Strain	SG+63CC
	Invert, Axial Strain	SG+63IA
	Invert, Circumferential Strain	SG+63IC
23 in. (584 mm) North of CL	Crown, Axial Strain	SG+23CA
	Crown, Circumferential Strain	SG+23CC
	Invert, Axial Strain	SG+23IA
	Invert, Circumferential Strain	SG+23IC
	East, Axial Strain	SG+23EA
	East, Circumferential Strain	SG+23EC
	West, Axial Strain	SG+23WA
	West, Circumferential Strain	SG+23WC
23 in. (584 mm) South of CL	Crown, Axial Strain	SG-23CA
	Crown, Circumferential Strain	SG-23CC
	Invert, Axial Strain	SG-23IA
	Invert, Circumferential Strain	SG-23IC
	East, Circumferential Strain	SG-23EC
	West, Circumferential Strain	SG-23WC
63 in. (1600 mm) South of CL	Crown, Axial Strain	SG-63CA
	Crown, Circumferential Strain	SG-63CC
	Invert, Axial Strain	SG-63IA
	Invert, Circumferential Strain	SG-63IC
82 in. (2080 mm) North of CL	Vertical String Pot	VSP+82
60 in. (1520 mm) North of CL	Vertical String Pot	VSP+60
30 in. (760 mm) North of CL	Vertical String Pot	VSP+30
10 in. (250 mm) North of CL	Vertical String Pot	VSP+10
At CL	Vertical String Pot	VSP0
10 in.(250 mm) South of CL	Vertical String Pot	VSP-10
30 in. (760 mm) South of CL	Vertical String Pot	VSP-30
60 in. (1520 mm) South of CL	Vertical String Pot	VSP-60
82 in. (2080 mm) South of CL	Vertical String Pot	VSP-82
Crown	Horizontal String Pot	HSP_C
Invert	Horizontal String Pot	HSP_I
South End Cap	Pressure Sensor	Pressure Sensor 1
South End Control Valve	Pressure Sensor	Pressure Sensor 2
South End Cap	Flow Meter	Pressure Sensor 3
Above Specimen	200 Kip Load	200Kip_Disp
Above Specimen	200 Kip Displacement	200Kip_Load

1 in. = 25.4 mm

4.4. Experimental Results

The following section provides results from the Bionax SR four-point bending test. Measurements of vertical displacement, applied load, and joint rotation are reported, followed by the moment-rotation relationship for the restrained joint. No leakage of the joint was observed at any time before failure of the pipe.

4.4.1. Applied Vertical Displacement and Actuator Load

Vertical displacement was imposed in four steps. Figure 4.4 shows the vertical displacement at loading points versus time. Figure 4.5 shows the applied vertical load versus time. The first 2.5 in. (64 mm) of displacement occurred due to self-weight deflection of the specimen when the support jacks were removed. As shown in Figure 4.5, loading began at 300 seconds, when the crosshead was released. At a vertical displacement of 13.3 in. (338 mm), corresponding to an experiment time of 660 seconds, loading was paused to allow survey measurements along the pipe springline. Some reduction in loading occurred during the pause, as is evident in Figure 4.5. Loading continued at 1290 seconds up to a vertical displacement of 18.5 in. (470 mm). After a brief 35 second pause (1410-1445 seconds), constant loading was continued under servo control to a total imposed vertical displacement of 24.3 in. (617 mm).

At $t = 1650$ seconds, an abrupt increase in actuator load from 1.3 kips (5.8 kN) to 1.5 kips (6.7 kN) is shown in Figure 4.5. This change in load occurred when the north and south support saddles slipped from their supporting rollers. The test specimen remained stable and loading was continued without pausing. It should be noted that, after this point in the test sequence [vertical displacement equal to 22 in. (560 mm)], the north and south support points were not able to move laterally, thus altering the test boundary conditions.

Figure 4.6 shows the vertical spring pot (VSP) displacements measured along the pipe at six increments of imposed displacement. The figure shows good agreement between string pots positioned at equal distances on either side of the test centerline. Note that VSP+60 and VSP-60 reached the end of their measurement strokes at about 20 in. (508 mm). Also shown in the figure are survey measurements, taken with a total station instrument, along the springline of the specimen during the pause at 13.4 in. (340 mm) of applied vertical displacement. These survey measurements are in excellent agreement with the string pot measurements.

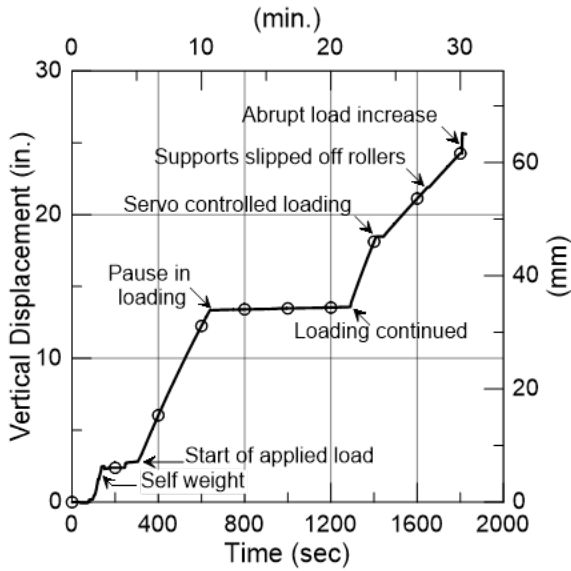


Figure 4.4. Vertical displacement at loading points vs. time

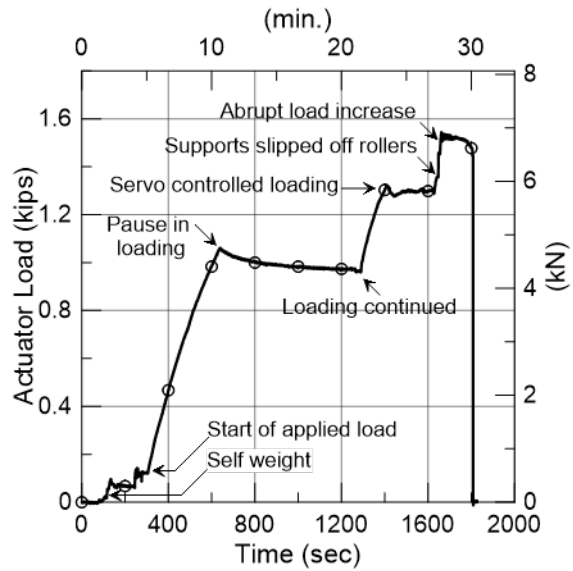


Figure 4.5. Actuator load vs. time

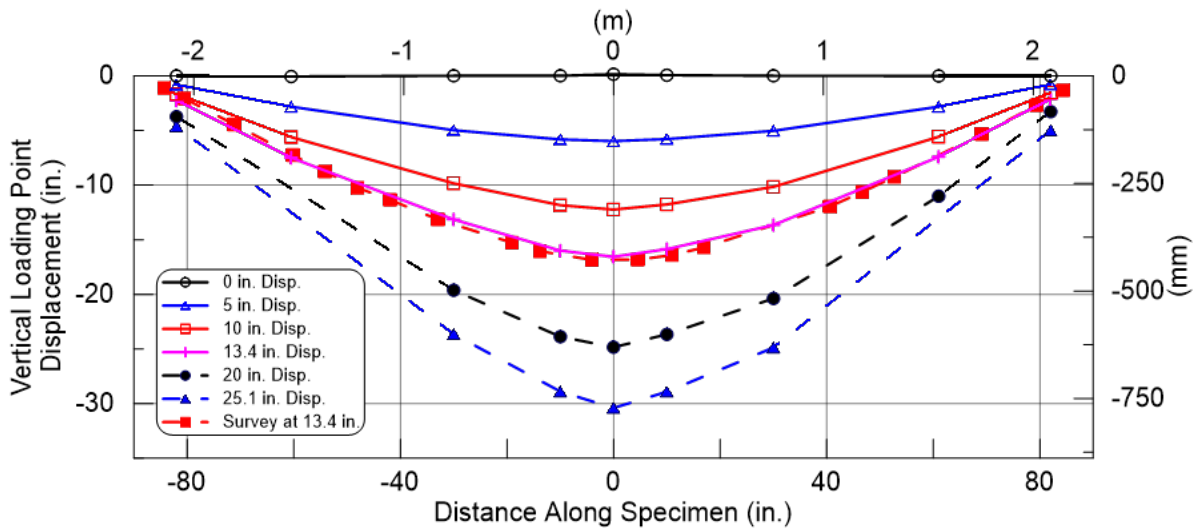


Figure 4.6. Vertical displacements along the pipe specimen for various vertical load point displacements

4.4.2. Bending Test Strains

Strains were measured at four planes along the bending test specimen. Figure 4.7 shows the axial and circumferential strain gages measurements at the crown and invert of the specimen for strain gage planes SG+63 and SG-63. These planes are positioned approximately halfway between the loading and support points along the barrel of the pipe, as shown in Figure 4.1. The figure demonstrates the symmetry and consistency in measurements among gages placed at equal

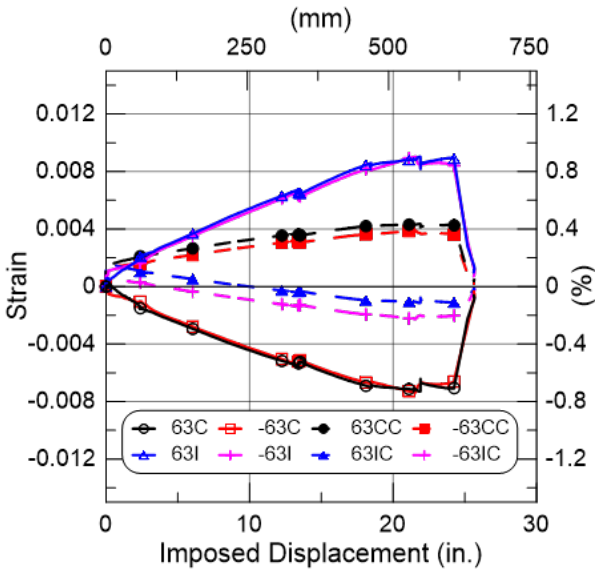


Figure 4.7. Axial and circumferential strains at the crown and invert for planes SG+63 and SG-63

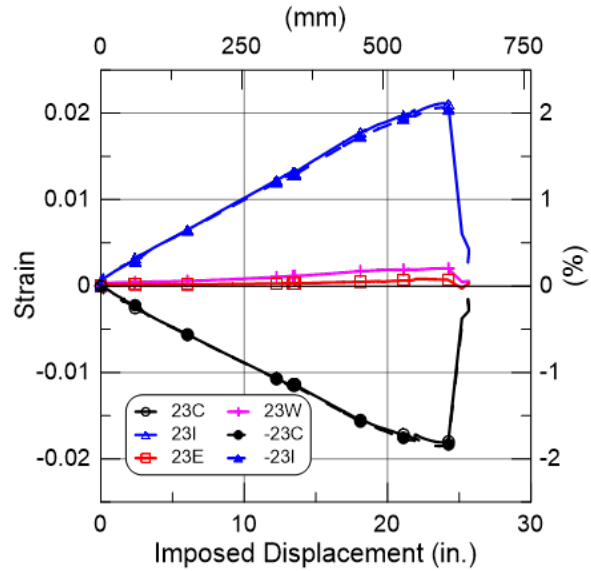


Figure 4.8. Axial strains at the specimen crown, invert, and springlines for planes SG+23 and SG-23

distances along the spigot and bell sections of the pipe. Figure 4.8 provides axial strain gage measurements at the crown, invert, and springlines for gage planes SG+23 and SG-23. Maximum axial tensile strains of approximately 2.1% were recorded at the pipe invert while maximum compressive strains of -1.8% were measured at the crown. The low levels of tensile strain at the SG+23 east and west springlines are indicative of a shift in neutral axis and geometric extension of the pipe between loading points.

Figure 4.9 and Figure 4.10 provide the crown and invert strains, respectively, at several levels of imposed vertical displacement. The figures show relatively symmetrical measurements at equal distances on either side of the joint. The first few displacement levels show that SG±63 axial strains are about one-half of those measured at SG±23. After about 13 in. (330 mm) of imposed displacement, the strains measured between the loading points increased more rapidly than those located outside of the constant moment region.

4.4.3. Restrained Joint Moment-Rotation

The moment-rotation response of the restrained joint is provided in Figure 4.11. Rotation (or deflection) of the specimen is calculated simply as the arcsine of vertical displacement at VSP-30 or VSP+30 divided by the distance along the pipe from the end support to the vertical loading

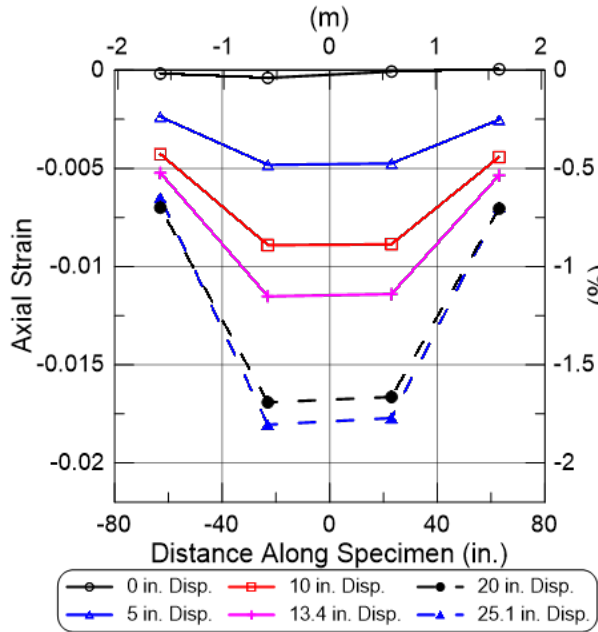


Figure 4.9. Crown strain at various levels of loading point vertical displacement

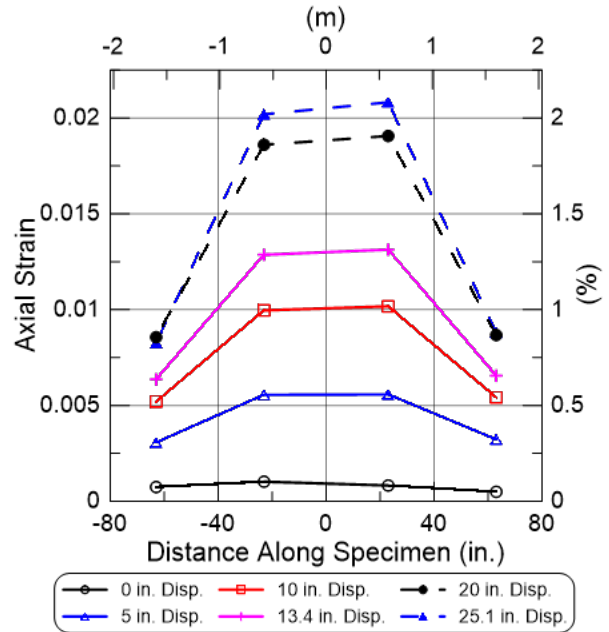


Figure 4.10. Invert strain at various levels of loading point vertical displacement

point. As shown in Figure 4.6, the vertical displacements of the pipe from either VSP-30 or VSP+30 to the end support can be represented by a linear trend that is the same on the north and south ends of the pipe. The deflection, or relative rotation, which is plotted in Figure 4.11, is the sum of the VSP rotations calculated with respect to both VSP-30 and VSP+30. This deflection represents the effective rotation of those pipe segments outside the center segment where the pipe experiences its maximum curvature between the vertical support points.

The moment in Figure 4.11 is approximated under the assumptions of idealized beam theory from the load applied by the test frame, P , and distance from support point to loading point, l_s , as

$$M = \frac{P l_s}{2} \quad (4.1)$$

where l_s is equal to 60 in. (1.5 m), as shown in Figure 4.1. The moment reported in the figure also includes the contributions of pipe self-weight and weight of water.

The moment-rotation relationship in Figure 4.11 increases at an approximately linear rate until about 25 degrees. After the pause in loading at 25 degrees, the slope of the moment versus rotation plot decreases until approximately 43 degrees. At this rotation the support points slipped, as

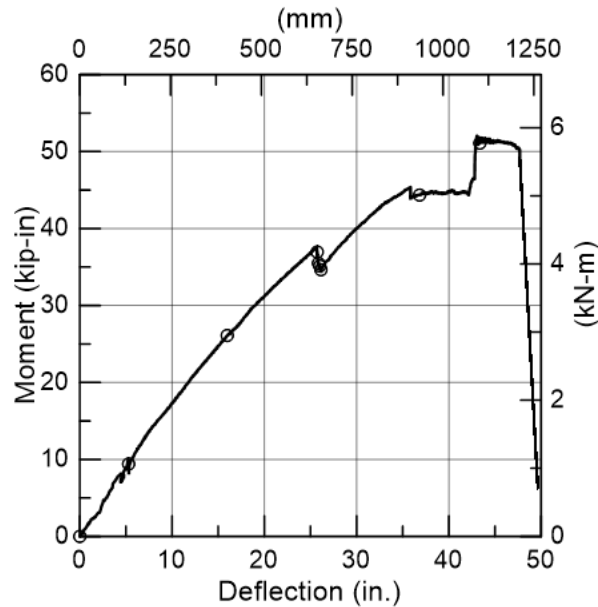


Figure 4.11. Applied moment vs. specimen deflection

previously discussed, disrupting the boundary conditions of the test. At 43 degrees the maximum moment spikes at 52 kip-in. (5.9 kN-m), after which failure of the bending test specimen occurred at 47.5 degrees.

4.4.4. Specimen Deflection

Figure 4.12 shows a sequence of photos of the test specimen before, during, and following the four-point bending test, including pipeline deformation at applied vertical displacements of the pipeline centerline of 13.4 in. (340 mm), 18.5 in. (470 mm), and maximum of 25 in. (635 mm), just before pipe failure. It should be recognized that there is some distortion in the photos due to the fisheye effect of the camera lens. Nevertheless, this sequence of photos shows the remarkable degree of deflection that the pipeline was able to sustain before failure. A relative rotation of 47 degrees is shown in Figure 4.12d, consistent with the largest deformation attained by the test specimen. This photo provides an illustration of how the relative rotation, as described previously in Section 4.4.3, is defined.

Figure 4.13 and Figure 4.14 show the pipeline after failure. Figure 4.13 is a photo of the test specimen immediately after failure. Figure 4.14 is a close-up photo of the pipeline joint between

the restraining collars. Full circumferential failures at both sides of the pipe just outside the restraints are visible in the photo.



(a) Initial position



(b) 13.4 in. (340 mm) vertical displacement



(c) 18.5 in. (470 mm) vertical displacement (beginning of servo control)



(d) 25 in. (635 mm), just before failure

Figure 4.12. Restrained joint at several levels of imposed bending deformation

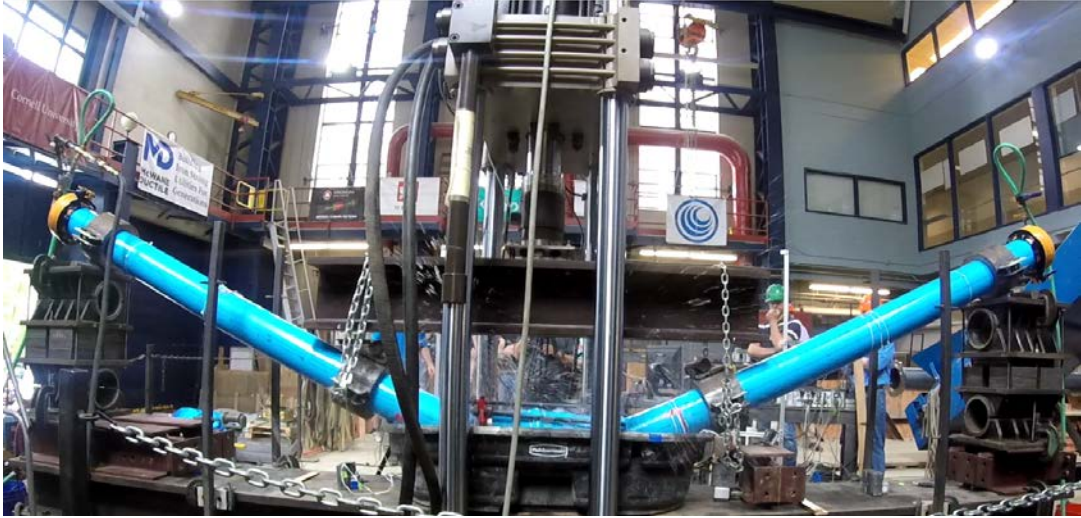


Figure 4.13. Restrained joint bending test failure



Figure 4.14. Failure of specimen at both the north and south restraints

4.5. Four-Point Bending Test Conclusions

A four-point bending test was performed on an 18-ft (5.5-m)-long section of Bionax SR pipe with the restrained bell and spigot joint centered on the frame. Loading points were positioned 30 in. (0.76 m) on either side of center. The pipe was pressurized with approximately 80 psi (550 kPa) of water throughout the test. The first vertical displacement of 2.5 in. (64 mm) was due to the self-weight of the pipe when support jacks were removed. Initial loading was applied solely through

the downward movement of the crosshead with a pause at 13.3 in. (338 mm) to survey the springline. After 18.5 in. (470 mm) of vertical displacement, the crosshead was locked and additional loading was applied using the 6 in. (152 mm) stroke MTS actuator until failure at a total vertical displacement of 24.3 in. (617 mm).

A maximum moment of 52 kip-in. (5.9 kN-m) occurred at a deflection of 43 degrees. There was a reduction in moment for the remainder of the test until failure at maximum rotation of 47.5 degrees. As shown by the photos and test measurements, the joint was able to sustain significant deformation without leakage or loss of internal pressure before failure.

Section 5

Axial Pull Tests

This section summarizes the results of four axial pull tests to evaluate the axial resistance of nominal 6-in. (150-mm)-diameter Bionax SR PVCO pipe with extended bells and restraints to relative axial movement between the pipe and adjacent soil. The tests were performed at three soil depths to crown of pipe, including 30, 45, and 60 in. (760, 1140, and 1520 mm). During each test the pipe was pulled approximately 30 in. (760 mm) through the soil. Three tests were conducted with Ford Meter Box Type 1559 restraints. The fourth test was conducted at a depth to top of pipe of 45 in. (1140 mm) with Ford Meter Box Type 1309 restraints. A description of the restraints is provided in Section 1.4, and photos and transverse cross-sections of the restraints are in Figure 1.3. This section describes the setup, testing procedure, and measured pipeline response for all four axial pull tests.

5.1. Test Layout and Instrumentation

The tests were performed at the north end of the Cornell large-scale split basin. Figure 5.1 shows a plan view of the testing setup. In all tests the bell mouth was facing south. The total length of the joint specimen buried in soil was 147.5 in. (3750 mm), with a distance of 64.7 in. (1620 mm) from the north restraining collar to the north inside boundary of the split basin. The joint was set to open 2.5 in. (63.5 mm) before engagement of the joint restraint. This initial setup was achieved through careful measurements of the distances between the nuts on the restraining rods and the restraining collar to ensure uniformity in the axial movement at all six rod locations.

As previously stated, the purpose of the tests was to assess the resistance of the pipeline, joint, and restraints to relative axial slip between the test specimen and adjacent soil. This resistance depends predominantly on the geometry of the pipeline system, depth, and soil strength. Because it is not influenced in a significant way by internal pipe pressure, the tests were conducted under zero internal pressure.

A stiff loading frame was connected to the north end of the split basin. The pipe was gripped at the outside of the basin with three UFR 1559 restraints provided by Ford Meter Box. Load was applied through rods connecting the restraints to an MTS servo-controlled hydraulic actuator mounted on the end of the frame. The actuator had a 10 in. (254 mm) stroke and a capacity of 22

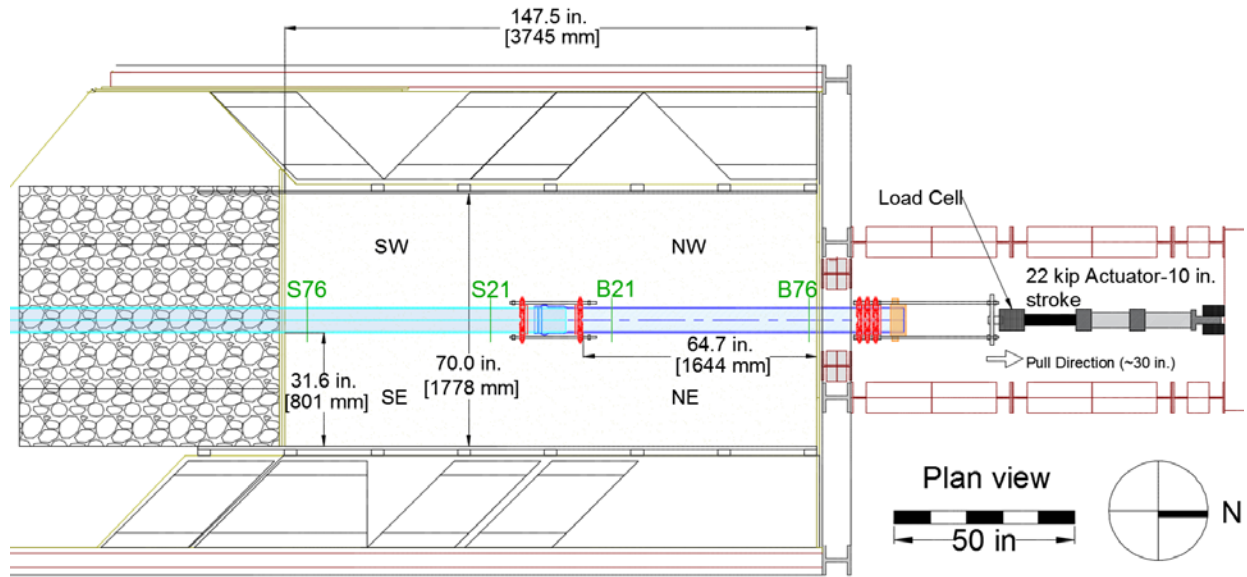


Figure 5.1 Plan view of pull through specimen including approximate locations of nuclear densitometer and moisture content measurements

kip (98 kN). Load was recorded through a 55 kip (245 kN) load cell located between the actuator and pipe.

A loading rate of one in. (25.4 mm) per minute was used. After a 10 in. (254 mm) pull was completed, the system was unloaded. The actuator was moved south 10 in. (254 mm), and the process was repeated until three full cycles [approximately 30 in. (762 mm) in total] were completed. During this process, data were acquired at 2 Hz during loading and unloading, and 0.1 Hz during reset.

Table 5.1 summarizes the instrumentation for each test. There were four planes of strain gages on each test specimen. Two planes were on the bell and spigot sides of the joint, respectively. The two planes on the bell side were labeled B21 and B76 being approximately 21 and 76 in. (533 and 1930 mm) from the bell face, respectively. Similarly, the spigot planes were labeled S21 and S72, following the aforementioned procedure.

String potentiometers, referred to as horizontal string pots (HSPs) in this section, were used to measure pipe displacements, as well as joint opening. HSP_North was mounted on the North face of the box, and measured pipe displacement as it is pulled out of the box (i.e., leading edge displacement). HSP_North_Grip was attached to the northern edge of the pipe to check for slip

Table 5.1. Instrumentation for IPEX pull-through tests

Location	Instrument	Local Instrument Name
22 Kip. Actuator	Internal Actuator LVDT	MTS 22KIP DISP
South End of Actuator	55 kip. Load Cell	MTS_55KIP_LOAD
North End of Box	String Pot	HSP_North
Loading Restraints	String Pot	HSP_North_Grip
North Edge of Spigot	String Pot	HSP_Joint_Open
South End of Spigot	String Pot	HSP_South
76 in. North of Bell Face	Crown, Axial Strain	B76C
76 in. North of Bell Face	Invert, Axial Strain	B76I
21 in. North of Bell Face	Crown, Axial Strain	B21C
21 in. North of Bell Face	Crown, Circumferential Strain	B21CC
21 in. North of Bell Face	East Springline, Axial Strain	B21E
21 in. North of Bell Face	West Springline, Axial Strain	B21W
21 in. North of Bell Face	Invert, Axial Strain	B21I
21 in. North of Bell Face	Invert, Circumferential Strain	B21IC
21 in. South of Spigot Face	Crown, Axial Strain	S21C
21 in. South of Spigot Face	Invert, Axial Strain	S21I
21 in. South of Spigot Face	East Springline, Axial Strain	S21E
21 in. South of Spigot Face	West Springline, Axial Strain	S21W
76 in. South of Spigot Face	Crown, Axial Strain	S72C
76 in. South of Spigot Face	Invert, Axial Strain	S72I

(1 in. = 25.4 mm)

between the pipe and loading restraints. HSP_Joint_Open was epoxied inside the spigot and connected to the bell to monitor joint opening. It was used to confirm that the joint opened fully during each test. HSP_South was mounted at the southern end of the test setup, and was connected to the spigot outside the plywood wall at the southern end of test setup. This string pot measured displacement of the spigot as the test pipeline was pulled through the soil (i.e., trailing edge displacement).

5.2. Soil Placement and Compaction

The soil used during the axial pull tests was a crushed, washed, glacio-fluvial sand produced by RMS Gravel consisting of particles mostly passing the ¼ in. (6.35 mm) sieve. Figure 5.2 is a grain

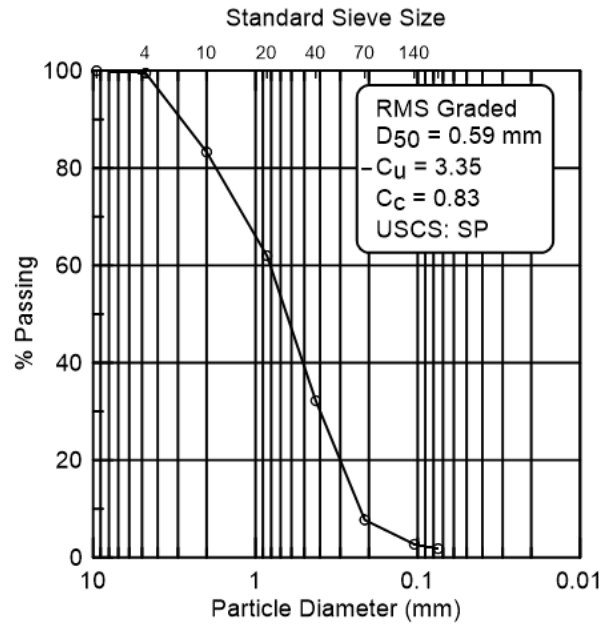


Table 5.2. PT45 Compaction Data

Location	Dry Unit Weights (lb/ft ³) ^a						Moisture Tin Water Content, w (%)					
	Lift 1	Lift 2	Lift 3	Lift 4	Lift 5	Lift 6	Lift 1	Lift 2	Lift 3	Lift 4	Lift 5	Lift 6
NW	106.1	109.8	107.1	107.4	106.6	105.7	5.9	2.8	3.6	4.9	4.9	4.6
NE	106.5	109.6	108.8	109.7	107.2	105.9	5.2	3.3	3.5	4.0	3.6	4.4
SW	106.5	108.2	106.3	106.3	106.8	107.3	4.2	4.6	4.1	5.9	5.9	4.2
SE	105.2	111.1	106.7	107.8	106.6	105.7	4.2	4.0	3.9	3.7	4.3	4.4
Avg	106.1	109.7	107.2	107.8	106.8	106.1	4.9	3.7	3.8	4.6	4.7	4.4
Stdev	0.6	1.2	1.1	1.4	0.3	0.8	0.8	0.8	0.3	1.0	1.0	0.1
Global Avg	107.3						4.3					
Global Stdev	1.5						0.8					

5.2.2. Axial Pull Test 2 (PT30): 30 in. Burial

Five lifts of soil were placed to achieve the desired depth of 30 in. (762 mm) to top of pipe. Table 5.3 lists soil unit weight and moisture content data for each lift as well as standard deviations among the lifts.

Table 5.3. PT30 Compaction Data

Location	Dry Unit Weights (lb/ft ³)					Moisture Tin Water Content, w (%)				
	Lift 1	Lift 2	Lift 3	Lift 4	Lift 5	Lift 1	Lift 2	Lift 3	Lift 4	Lift 5
NW	102.9	109.7	108.0	111.1	100.4	3.9	3.7	3.5	3.6	3.8
NE	102.7	109.8	106.7	106.4	104.1	3.9	3.6	3.4	3.5	3.6
SW	102.1	109.5	103.9	110.1	104.0	3.9	3.9	3.7	3.5	3.8
SE	103.7	108.7	104.9	110.2	105.0	3.9	3.5	3.5	3.4	3.3
Average	102.8	109.4	105.9	109.5	103.4	3.9	3.7	3.5	3.5	3.6
Stdev	0.6	0.5	1.8	2.1	2.0	0.0	0.2	0.1	0.1	0.2
Global Average	106.2					3.7				
Global Stdev	3.2					0.2				

5.2.3. Axial Pull Test 3 (PT45b): 45 in. Burial, 1309 Restraint

The pipe was placed on a 13 in. (330.2 mm) bed of soil. This test was performed with the Ford Meter Box Type 1309 restraints. Six lifts of soil were added to achieve the desired depth of 45 in. (1143 mm). Table 5.4 shows compaction data and moisture content for each lift as well as standard deviations among the lifts.

Table 5.4. PT45b Compaction Data

Location	Dry Unit Weights (lb/ft ³) ^a						Moisture Tin Water Content, w (%)					
	Lift 1	Lift 2	Lift 3	Lift 4	Lift 5	Lift 6	Lift 1	Lift 2	Lift 3	Lift 4	Lift 5	Lift 6
NW	106.5	107.8	108.9	108.0	111.0	107.5	4.5	4.5	3.2	4.1	0.2	3.7
NE	101.7	107.6	109.0	106.4	110.7	107.9	8.5	4.5	3.9	4.3	0.1	3.9
SW	108.0	107.8	108.9	108.0	109.8	107.6	3.1	3.3	3.3	3.5	0.9	4.1
SE	107.1	106.9	107.9	107.0	112.5	109.1	3.0	3.5	3.2	3.9	0.1	3.5
Average	105.8	107.5	108.7	107.3	111.0	108.0	4.8	3.9	3.4	3.9	0.3	3.8
Stdev	2.8	0.4	0.5	0.8	1.1	0.7	2.6	0.6	0.3	0.3	0.4	0.3
Global Average	108.1						3.4					
Global Stdev	2.0						1.8					

5.2.4. Axial Pull Test 4 (PT60): 60 in. Burial

Six lifts of soil were placed to achieve the desired depth of 45 in. (1140 mm) to top of pipe. To attain a simulated 60 in. (1520 mm) burial depth, iron and steel weights, evenly distributed across the soil surface, were used to develop confining pressure at the depth of pipe equivalent to that with an additional 15 in. (380 mm) of soil. Sheets of 0.75-in. (19-mm)-thick plywood were placed atop the soil to promote uniform weight distribution. Table 5.5 lists soil unit weight and moisture content data for each lift as well as standard deviations among the lifts.

5.3. Axial Pull Forces and Displacements

This section summarizes the axial pull forces and displacements measured in the four axial pull tests. The 1559 joint restraint was used in Tests 1, 2, and 4 at burial depths to pipe crown of 30, 45, and 60 in. (760, 1140, and 1520 mm), respectively. Test 3 was performed with the 1309 joint restraint at a burial depth to pipe crown of 45 in. (1140 mm).

Table 5.5. PT60 Compaction Data

Location	Dry Unit Weights (lb/ft ³) ^a						Moisture Tin Water Content, w (%)					
	Lift 1	Lift 2	Lift 3	Lift 4	Lift 5	Lift 6	Lift 1	Lift 2	Lift 3	Lift 4	Lift 5	Lift 6
NW	106.6	109.5	107.6	105.8	108.6	110.2	3.5	3.6	3.6	3.4	3.0	3.1
NE	107.1	108.2	107.1	107.9	107.0	110.2	3.5	3.4	3.5	3.7	2.9	2.8
SW	105.8	109.0	106.2	106.5	108.5	107.6	3.5	3.9	4.3	3.2	2.9	3.1
SE	108.0	106.3	106.5	106.9	108.7	108.2	3.7	2.8	4.0	3.0	3.1	3.5
Average	106.9	108.2	106.9	106.8	108.2	109.0	3.5	3.4	3.8	3.3	3.0	3.1
Stdev	0.9	1.4	0.6	0.8	0.8	1.3	0.1	0.5	0.4	0.3	0.1	0.3
Global Average	107.7						3.4					
Global Stdev	1.3						0.4					

5.3.1. Interpretation of Measurements

As shown in Figure 5.1 the strain gages at plane B76 provide a measure of load that should closely match the actuator load. At plane B21 and S21 the strain gage data provide a measure of load at the leading and trailing edge of the joint restraint, respectively, as it is pulled axially through the soil. The difference in axial load between planes B21 and S21 is the load that is dropped across the restraint. As this load increases there is more resistance to movement, and thus higher force mobilized in the pipeline that may limit the amount of axial ground deformation the pipeline can accommodate before failure.

The axial pull tests mobilized strains exceeding 1% in the pipe, thus deforming the PVCO into the range of nonlinear stress vs strain behavior. To determine the force in the pipe at the strain gage planes, it is necessary to use the axial secant modulus of the PVCO that is compatible with the axial strain mobilized in the pipe during the time of measurement. Using stress versus strain data from tensile coupon tests previously performed for IPEX (Stewart et al., 2013a), the ratio of axial secant modulus to initial elastic modulus is plotted as a function of axial strain in Figure 5.3. Please note that at 1% strain, or 0.01, the figure shows about a 10% decline relative to the initial modulus associated with very low levels of strain.

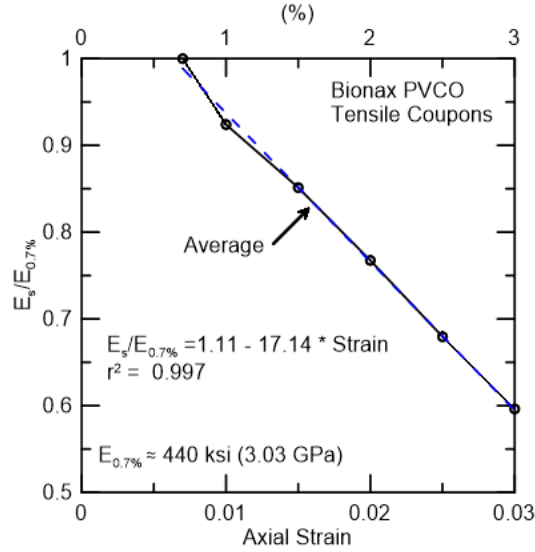


Figure 5.3. Ratio of axial secant modulus to elastic modulus vs. axial strain

Because the IPEX PVCO is a transversely anisotropic material (Wham et al., 2017), the calculation of axial load in the pipe should account for the transversely anisotropic properties. The axial stress in a transversely isotropic solid under plane stress conditions is given by Bower (2010), and is expressed in cylindrical coordinates for pipe as follows

$$\sigma_l = \frac{E_l(\varepsilon_l + \varepsilon_\theta \nu_{\theta l})}{(1 - \nu_{l\theta} \nu_{\theta l})} \quad (5.1)$$

where σ_l is the axial stress, E_l is axial secant modulus, ε_l is the axial strain, ε_θ is the circumferential strain, $\nu_{\theta l}$ is Poisson's ratio for the effect of strain caused by circumferential stress on the longitudinal strain, and $\nu_{l\theta}$ is Poisson's ratio the strain caused by stress in the longitudinal direction on the resulting strains in the circumferential direction

The axial force, F_A was calculated as $F_A = \sigma_l A$, where σ_l is derived from Eqn. 5.1 and A is the cross-sectional area of the pipe for tests T1, T2, and T4. The axial force in T3 used Hooke's law for uniaxial tension since the circumferential strain gages did not survive.

The leading end displacement at the north end of the pipe relative to the north end of the split basin was measured with string pot HSP North. This displacement includes elongation of the pipe caused by axial pull forces. The elongation between the grip and B21 was estimated by taking the axial load difference between the load cell and B21 and adjusting for friction mobilized between the pipe and soil to calculate the elastic pipe elongation with a strain compatible secant modulus

from Figure 5.3. For a constant frictional force per length of pipe, consistent with the burial conditions of the test, approximately half the load difference is the average load causing elongation of the pipe. The estimated elongation from the average pipe load is small, with a maximum of about 0.25 in. (6.4 mm). Since the maximum displacement of the north edge of the pipe during the tests was nearly 30 in. (760 mm), a correction for the elongation of the pipe caused by axial pull forces is less than 1% of this measurement. Thus, the north end displacement of the pipe is very close to the axial movement near the joint at B21.

5.3.2 Axial Pull Test 1 (PT45): 45 in. (1140 mm) Burial Results

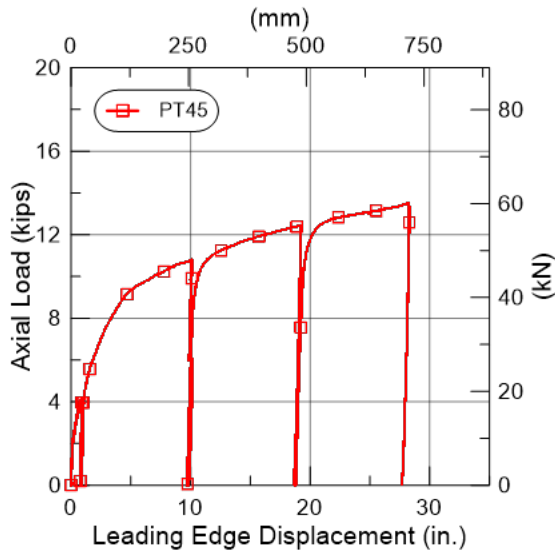
Figure 5.4a shows a plot of the load cell force versus the axial pullout displacement of the pipe measured by the actuator. Figure 5.4b shows the axial loads measured by the load cell and the strain gages at planes B76 and B21 versus the leading edge displacement of the pipe. As explained previously, after a 10 in. (254 mm) pull was completed, the pipe was unloaded and the actuator was moved south 10 in. (254 mm), and the process repeated until three full cycles of displacement. The axial force versus displacement plots are provided in the figure for all three cycles of displacement.

As expected, there is close agreement between the load versus displacement plots for the load cell and strain gages at B76. The axial force measured by the strain gages at B21 are lower than those at B76 because of the friction mobilized during pullout between the locations of B76 and B21. Thus, the difference between the loads at B76 and B21 represents the frictional force that developed along the bell portion of the test specimen.

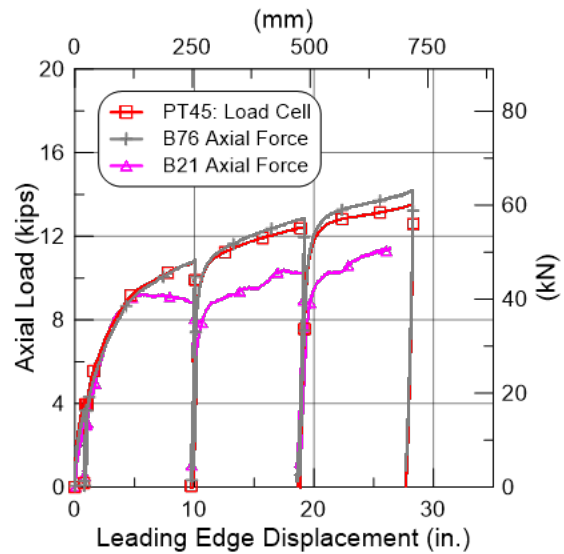
Strain gage measurements at S21 on the trailing edge of the restraint were very low for all tests, on the order of 0.5 kips (2.22 kN). The B21 axial force measured in Test 1 is 10 kips (44.5 kN) at 20 in. (510 mm) of leading edge displacement. Subtracting the axial force at B21 from that at S21 results in 9.5 kips (42.3 kN), which is the load drop across the joint. The B21 axial force is only about 5% higher than the actual load drop, and therefore is a good estimate of the axial load drop across the joint.

Figure 5.5 shows a photo of the minor to moderate cracking at the ground surface during this test. Such tensile cracking indicates that some volume expansion and shear distortion were transferred to the surface as the restrained pipe joint was pulled through the soil.

The string pot measurements indicate that the joint opened a maximum of 1.97 in. (50 mm) during the test, whereas the joint had been set to open 2.5 in. (64 mm). Figure 5.6 shows a photo of the



(a) Actuator load



(b) Load cell and strain gage loads

Figure 5.4. PT45 axial load vs. displacement plot for actuator, load cell, and strain gage loads

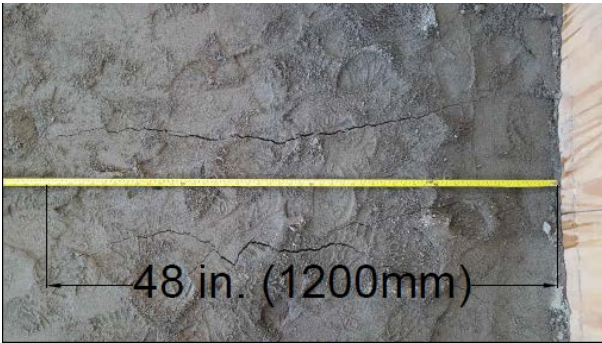


Figure 5.5. Soil surface cracking adjacent to north wall for PT45



Figure 5.6. Photo of sand lodged between nuts and collar of the joint restraint

restraint collar that was exposed when soil over the pipe was excavated after the pull test. Sand had lodged between the nuts and restraining collar along the rods, thereby preventing the full 2.5 in. (64 mm) of joint opening.

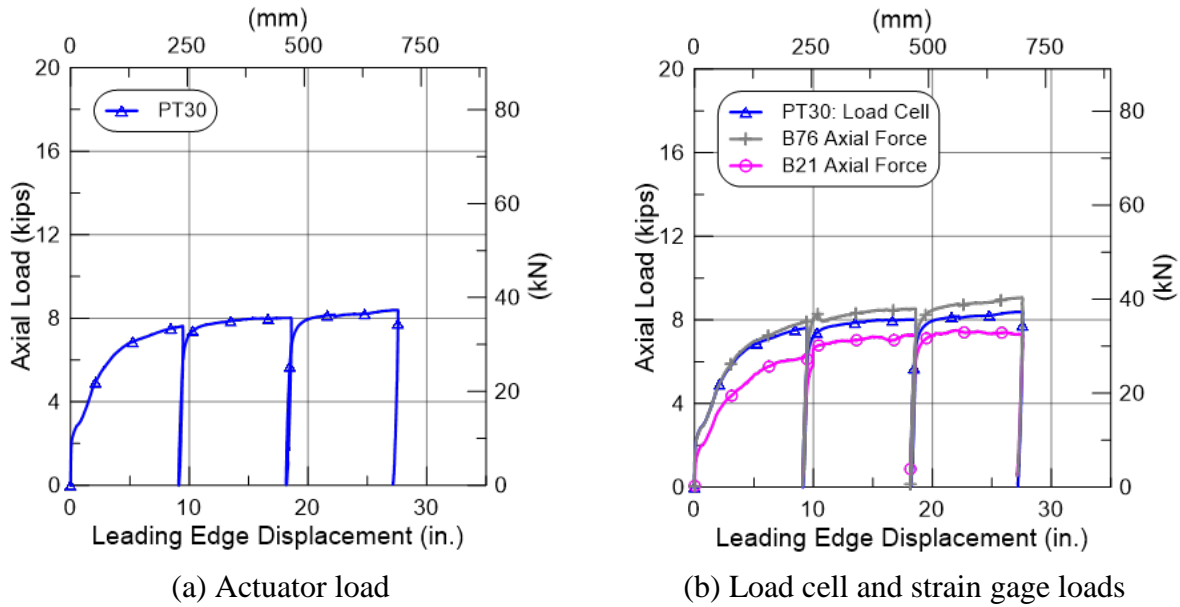


Figure 5.7. PT30 axial load vs. displacement plot for actuator, load cell, and strain gage loads

5.3.3 Axial Pull Test 2 (PT30): 30 in. (70 mm) Burial Results

Figure 5.7a shows a plot of the load cell force versus the axial pullout displacement of the pipe measured by the actuator, and Figure 5.7b shows the axial loads measured at by the load cell and by the strain gages at planes B76 and B21 versus the leading edge displacement of the pipe. As is the case for Figure 5.4, three cycles of displacement are plotted in the figure.

Again, there is close agreement between the load versus displacement plots for the load cell and strain gages at B76. The axial force measured by the strain gages at B21 are lower than those at B76 because of the soil friction mobilized, as discussed for Figure 5.4a. Again, the difference between the loads at B76 and B21 represents the frictional force that developed along the bell portion of the test specimen. For the same reasons as given for Figure 5.4, the B21 axial force is a good approximation of the axial load drop.

Figure 5.8 provides a photo of the surface cracks that appeared during this test. The cracking was more severe for this test relative to Test 1 and reflects volume expansion and shear distortion that develops as the restrained pipe joint is pulled through the soil. The greater width and severity of surface cracks are related to the lower depth of cover for this test

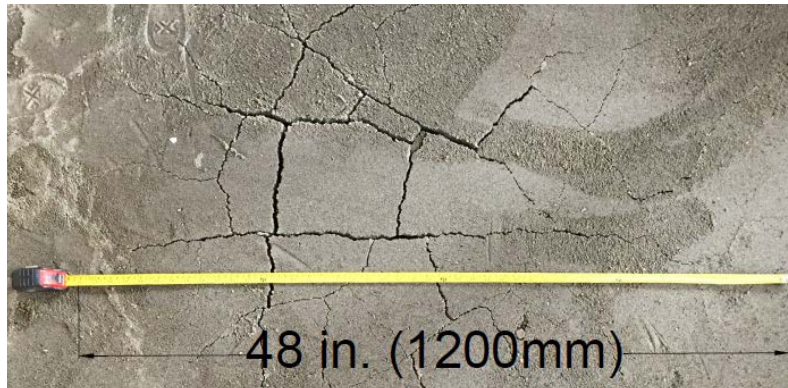


Figure 5.8. Soil surface cracking for PT30

The string pot measurements indicate that the joint opened a maximum of 2.15 in. (54 mm) during the test, whereas the joint had been set to open 2.5 in. (64 mm). When soil over the pipe was excavated after the pull test, sand was observed between the nuts and restraining collar of the joint in a manner similar that shown in Figure 5.6.

5.3.4 Axial Pull Test 3 (PT45b): 45 in. Burial 1309 Restraint Results

The axial load versus displacement plots for actuator and leading edge displacements are presented in Figure 5.9 for three cycles of displacement, similar to the plots for Tests 1 and 2. The loads developed in this test are lower at all levels of displacement than those in Test 1 even though the soil conditions and depth of burial are the same. The lower axial pull forces are related to smaller dimensions of the 1309 restraint relative to those of the 1559 restraint. At similar depths and displacements axial pull forces mobilized with the 1309 restraint are approximately 20% smaller than those generated by the 1559 restraint.

Surface cracking was not observed in this test even though minor to moderate cracking was observed for the 1559 restraint in Test 1 at the same depth. Apparently, the soil volume expansion and shear distortion associated with the smaller dimensions of the 1309 restraint were not sufficient to cause surface cracking.

The string pot measurements indicate that the joint opened a maximum distance of approximately 2.5 in. (54 mm) during the test, which compares well with the distance of 2.5 in. (64 mm) that was set at the beginning of the test. As shown in Figure 5.10, very little soil was observed between the face of the restraint and the nuts on the restraining rods. The 1309 restraint is equipped with only

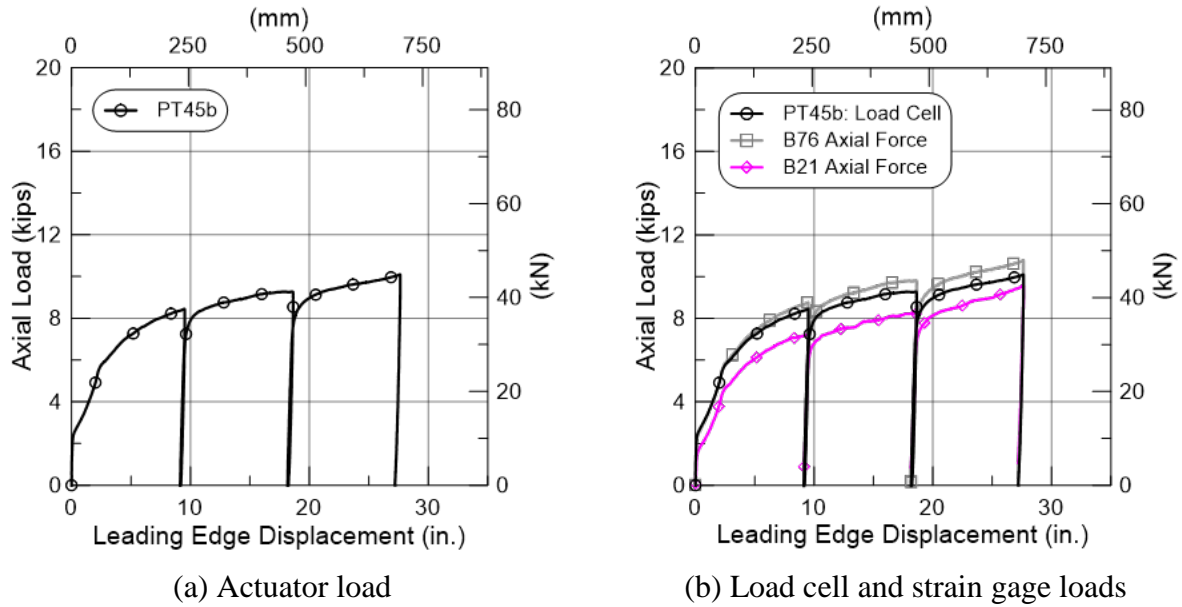


Figure 5.9. PT45b axial load vs. displacement plot for actuator, load cell, and strain gage loads



Figure 5.10. Joint opening post PT45b

two rods in comparison to the 1559 restraint with six rods. The smaller size and lower number of rods of the 1309 restraint reduces the opportunity for soil to become trapped between the nuts and restraint surface as the joint opens and the nuts make contact with the restraining collar.

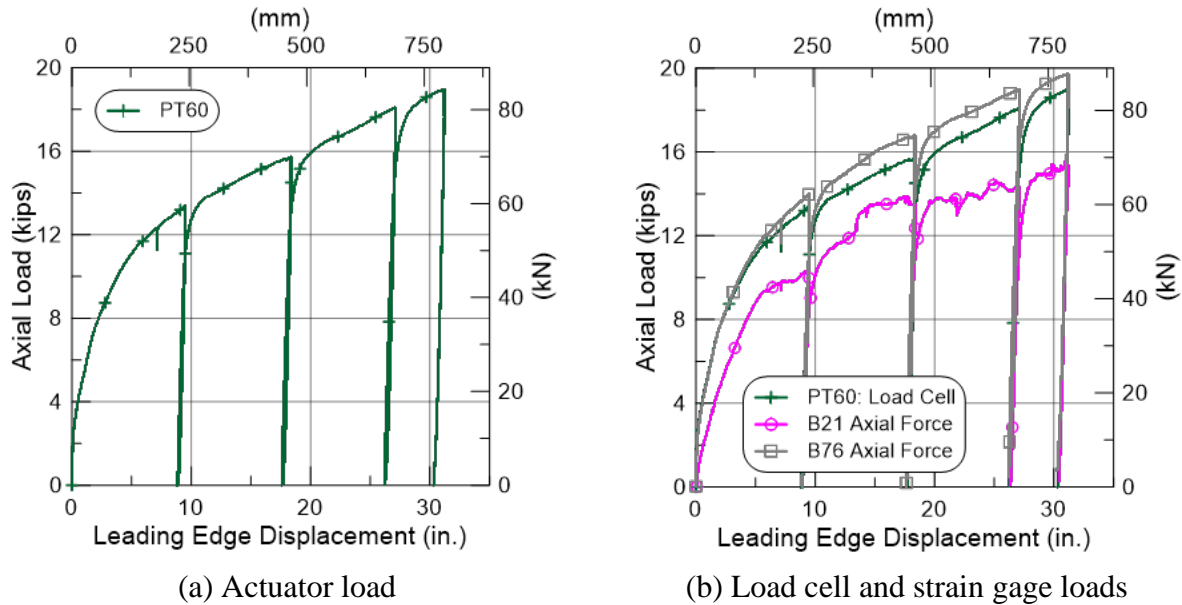


Figure 5.11. PT60 axial load vs. displacement plot for actuator, load cell, and strain gage loads

5.3.5 Axial Pull Test 4 (PT60): 60 in. Burial Results

As described previously, iron and steel weights, evenly distributed on plywood sheets on top of the soil surface, were used to simulate the additional confining pressure of 15 in. (570 mm) of soil for a total effective burial depth of 60 in. (1520 mm). The test specimen was pulled four times (Figure 5.11) for four cycles of axial displacement to attain a maximum axial movement of 30 in. (760 mm). A maximum force of nearly 19 kips (85 kN) was reached at a displacement of 31 in. (790 mm). It was not possible to confirm either the absence or presence of soil surface cracks because the plywood and surface weights prevented direct observation of the surface.

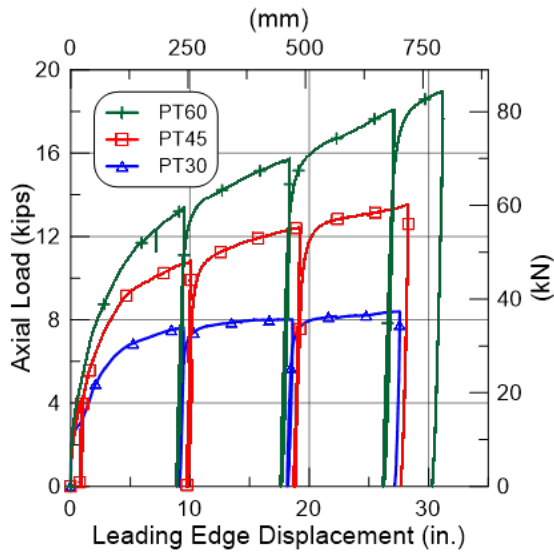
The pattern of load development with respect to displacement is similar to that observed in Tests 1 through 3. Again, there is close agreement between the load versus displacement plots for the load cell and strain gages at B76. The axial force measured by the strain gages at B21 are lower than those at B76 because of the friction mobilized during pullout between the locations of B76 and B21. The load measured at B21 is a good estimate of the axial load drop across the joint, as explained for Test 1.

5.4. Comparison of Axial Load vs Displacement Performance

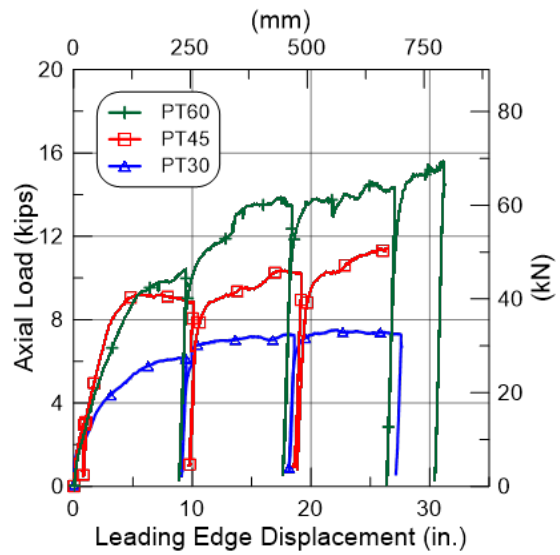
Figure 5.12 presents the axial load versus displacement plots for Tests 1 through 4 in a format where all the axial pull data can be compared side by side. Figure 5.12a and b show the actuator and B21 loads, respectively, plotted with respect to leading edge displacement. As discussed previously, the B21 axial load provides a good estimate of the load drop across the restrained joint because the load at S21 was very low in all tests at approximately 0.5 kips (2.2 kN). Also as previously discussed, the leading edge displacement is a good estimate of the axial movement at B21 near the restrained joint. Combining the B21 loads with the leading edge displacements in Figure 5.12b is equivalent to plotting the load drop across the restrained joints versus relative axial displacement between the restrained joint and soil. The successively higher load drops at increasingly deeper burial depths are shown clearly in this set of plots.

Figure 5.12c and d show the actuator and B21 loads for both the 1559 and 1309 restraints, respectively, plotted with respect to leading edge displacement in the same sand at the same 45-in. (1140-mm) depth to top of pipe. These figures provide for a direct comparison of the resistance to pullout of the two different restraints. As established above, Figure 5.12d is equivalent to plotting the load drop across the restrained joints versus relative axial displacement between the restrained joint and soil. The smaller 1309 restraint mobilizes only 80% of the resistance to pullout that the larger 1559 restraint generates.

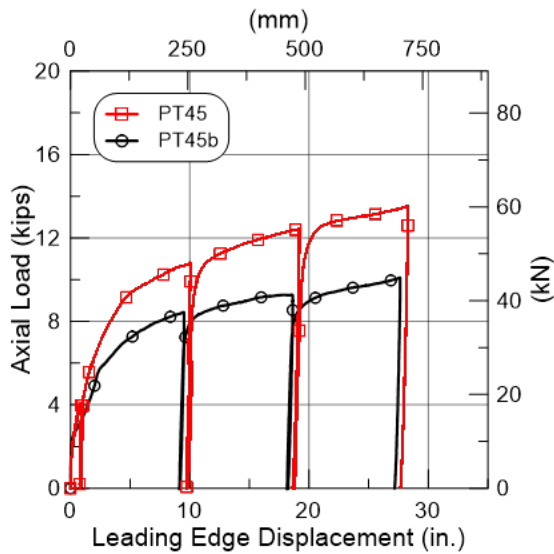
Figure 5.13 presents a plot of the B21 loads at 18 in. (460 mm) of displacement with respect to depth from the soil surface to centerline of pipe. These loads are approximately equal to the loads dropped across the restrained joints. A linear regression was fit to the data for pipes with the 1559 restraints at depths to pipe crown of 30, 45, and 60 in. (760, 1140, and 1520 mm). Although there are only three data points, the high coefficient of determination, $r^2 > 0.99$, provides confidence that the linear trend shown in the figure is statistically robust relative to the database. The linear regression has an intercept that is nearly zero, which is consistent with the axial resisting load mobilized by the restrained joint being directly proportional to depth, and thus the vertical confining stress provided by the soil. The single data point for the test involving the 1309 restraint is also shown on the plot. If a similar trend is inferred for the 1309 restraint, the axial resistance of pipe joints with 1309 restraints is expected to be 80% of the axial resistance of pipe joints with 1559 restraints at all depths in granular soil of similar density and strength.



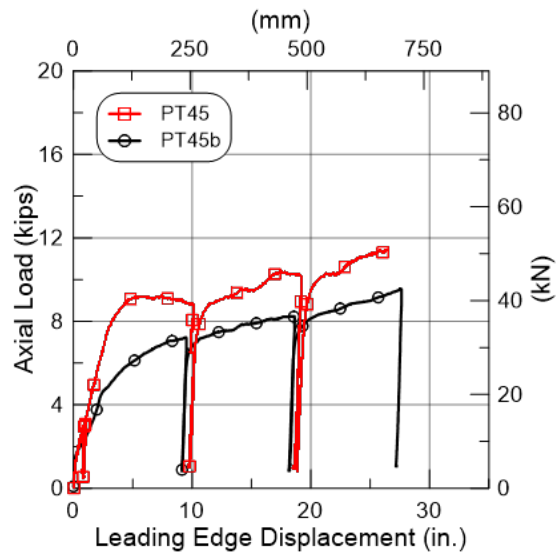
a) Actuator load vs. leading edge displacement for PT30, PT45 and PT60



b) B21 load vs. leading edge displacement for PT30, PT45 and PT60



c) Actuator load vs. leading edge displacement for PT45 and PT45b



d) B21 load vs. leading edge displacement for PT45 and PT45b

Figure 5.12. Comparison of axial load vs displacement measurements

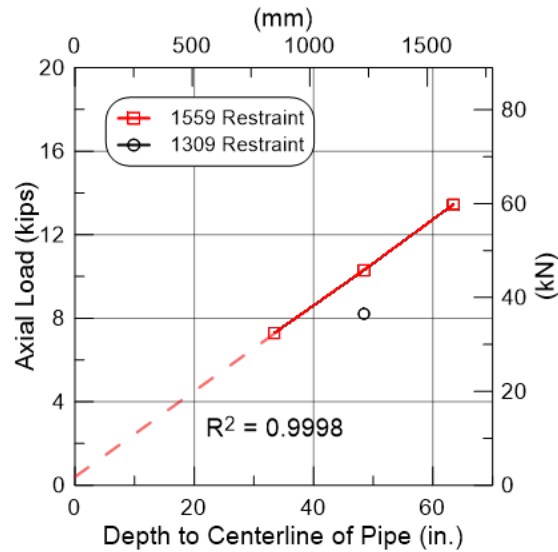


Figure 5.13. Axial load vs. depth to centerline of pipe

5.5. Axial Pull Tests Summary

Four axial pull tests were performed on restrained joints. Three tests were performed with the Type 1559 restraints at soil depths to crown of pipe of 30, 45, and 60 in. (760, 1140, and 1520 mm). The fourth test was conducted at a depth to top of pipe of 45 in. (1140 mm) with Ford Meter Box Type 1309 restraints. During each test the pipe was pulled approximately 30 in. (760 mm) through the soil.

Axial force vs displacement plots are presented and compared for the four tests in which the actuator load and axial load measured at 21 in. (533 mm) north of the bell face are plotted with respect to the leading edge displacement. Combining the axial loads measured at 21 in. (533 mm) north of the bell face with the leading edge displacements is equivalent to plotting the load drops across the restrained joint versus relative axial displacement between the restrained joint and soil. The successively higher load drops at increasingly deeper burial depths are shown clearly in the plots. The magnitude of resistance changes with relative displacement, and increases linearly with soil depth. The size of the restraint also affects resistance with the smaller 1309 restraint, generating 20% less axial force to pull through the soil than that required to pull the 1559 restraints at identical burial depths in the same soil.

Section 6

Fault Rupture Simulation

This section presents the results of a full-scale fault rupture test performed on a 6-in. (150-mm)-diameter Bionax SR pipeline with two restrained joints. The test was performed in the large-scale test basin at the Cornell University Large Scale Lifelines Testing Facility on June 6, 2017.

6.1. Experimental Setup

A plan view of the test layout, provided in Figure 6.1, shows the fault rupture plane and approximate locations of the four actuators generating basin movement. The pipeline consisted of three sections of Bionax SR pipe with two restrained joints (1559 restraints) positioned a distance of 120.5 in. (3.06 m) on each side of the fault. A 20-ft-(6.1-m)-long center section of pipe was placed such that the fault crossed the pipe midway between its spigot and bell ends. The intersection angle between the pipe and fault was 50°. The abrupt ground movement during the test was representative of a left-lateral strike-slip fault rupture as well as the most severe ground deformation that occurs along the margins of liquefaction-induced lateral spreads and landslides. The objective of the test was to evaluate the pipeline's ability to accommodate fault movement through axial extension and deflection of the pipe body and joints.

The pipeline was buried in the large-scale test basin at Cornell University in partially saturated sand, which was compacted to have an average friction angle of 42°, equivalent in strength to that of dense granular backfill. The 6.9-in. (175-mm) outer-diameter pipe was placed on a bed of soil with 13-in. (330-mm) thickness at the bottom of the test basin. The depth of burial to the top of pipe was 32 in. (800 mm) resulting in 52 in. (1320 mm) of total soil depth. During the test, the southern section of the basin remained stationary while the north end was displaced to the north and west by four large-stroke actuators to cause soil rupture and slip at the interface between the two parts of the test basin.

As presented in Figure 6.1, a total pipeline length of 34.4 ft (10.5 m) was buried in soil. The total pipeline length from the north to south inside walls of the test basin was 40.3 ft (12.3 m). The ends of the pipe were fixed to each end of the split basin to limit axial displacement or translation, representing worst-case loading conditions. Wooden retaining walls were located near the ends of the pipeline to allow access to instruments and end restraints. The pipe was pressurized with water

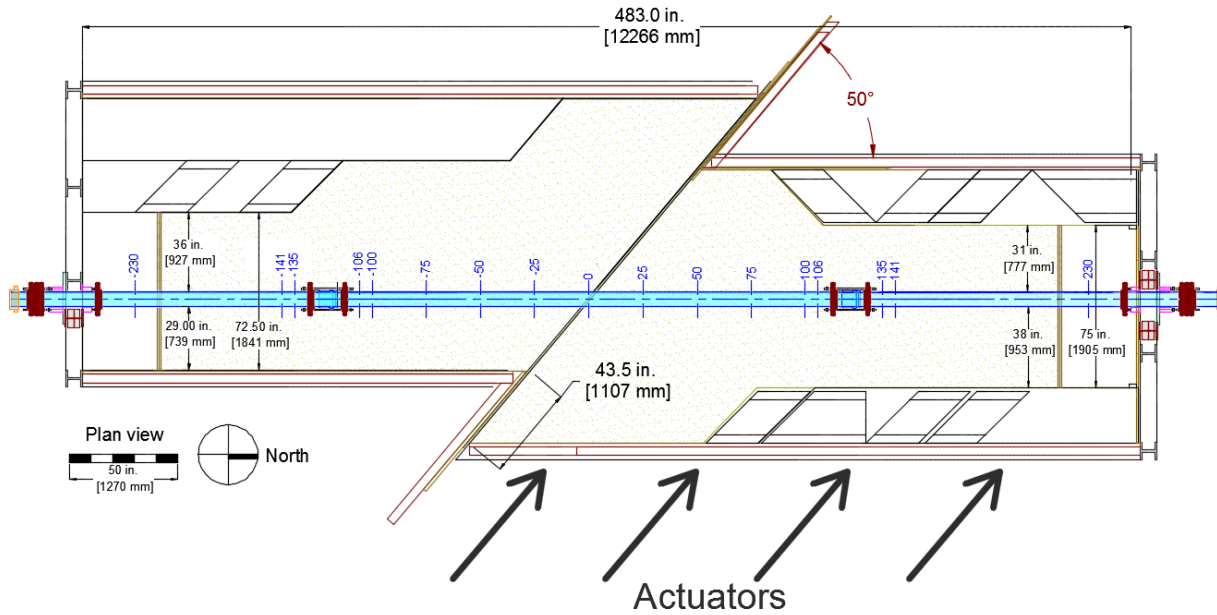


Figure 6.1. Plan view of split basin prior to fault rupture test

to approximately 80 psi (552 kPa). The north (movable) portion of the test basin was connected to four MTS hydraulic actuators with load cells controlled by a MTS Flextest GT controller. All actuators were operated in synchronized displacement control. The test configuration allows the actuators to displace the north half of the test basin a maximum of 43.5 in. (1105 mm) with a combined force of 510 kips (2270 kN).

6.1.1. Test Procedure

The general test procedure after instrument installation, soil placement, and filling the pipeline with water was:

- a) Begin data acquisition and start the servo-controlled hydraulic system
- b) Apply and verify internal water pressure
- c) Move the test basin 4 in. (100 mm) at a rate of 2 in./min (50 mm/min)
- d) Verify internal pressure and instrument response.
- e) Apply test basin movement until pipeline failure

6.1.2. Instrumentation

A total of 116 instruments were used to make various measurements during the test. The instrumentation included strain gages at specified locations (gage planes) along the pipeline, four load cells at each end of the specimen, and two digital transducers to measure internal water pressure. Measurements of the relative movement between the north and south sections of the test basin were gathered, including actuator force and displacement.

Figure 6.1 provides the locations of strain gage planes along the test specimen with respect to distance from the fault. Each gage number represents the distance (in inches) of the gage from the centerline of the specimen at the fault crossing. Positive (+) designation identifies gages north of the fault while negative (-) gages are positioned on the southern half of the test specimen. Gage planes were located at equal distances about the pipeline center. At each plane the circumferential positions of the gages and their orientations were identical with those at a counterpart location on the opposite side of the pipeline center. There were 88 strain gages installed at 19 planes to measure strains and evaluate axial forces and bending moments. Table 6.1 provides a list of each strain gage circumferential position [crown (C), invert (I), or east (E) or west (W) springline] and orientation [axial (A) or circumferential (C)].

Strain gage plane locations were chosen on the basis of the expected pipeline deformation, which was estimated by finite element simulation in combination with the results of the axial tension and four point bending test results, presented in Sections 2 and 4, respectively. Strain gage planes +230 and -230 provide measurements to evaluate the end loads. Strain gage planes close to the joints, ± 106 and ± 135 , measured strain concentration near the restraints.

Four calibrated load cells were positioned at each end of the test basin to measure axial load. Table 6.2 provides the locations and the labeling of the load cells. Three string potentiometers (string pots) were installed at each joint to measure pullout displacement and rotation. The string pot measurement system was protected by a joint shield composed of sheet metal that enclosed the joint. Figure 6.2 shows photos of the joint instrumentation and the protective metal enclosure.

Table 6.1. IPEX split basin strain gage instrumentation list

Location	Instrument Description	Local Instrument Name
210 in. South of FL	East, Axial Strain	SG-210EA
	West, Axial Strain	SG-210WA
141 in. South of FL	Crown, Axial Strain	SG-141CA
	Invert, Axial Strain	SG-141IA
	East, Axial Strain	SG-141EA
	East, Circumferential Strain	SG-141EC
	West, Axial Strain	SG-141WA
	West, Circumferential Strain	SG-141WC
135 in. South of FL	Crown, Axial Strain	SG-135CA
	Invert, Axial Strain	SG-135IA
	East, Axial Strain	SG-135EA
	East, Circumferential Strain	SG-135EC
	West, Axial Strain	SG-135WA
	West, Circumferential Strain	SG-135WC
106 in. South of FL	Crown, Axial Strain	SG-106CA
	Crown, Circumferential Strain	SG-106CC
	Invert, Axial Strain	SG-106IA
	Invert, Circumferential Strain	SG-106IC
	East, Axial Strain	SG-106EA
	East, Circumferential Strain	SG-106EC
	West, Axial Strain	SG-106WA
	West, Circumferential Strain	SG-106 WC
100 in. South of FL	Crown, Axial Strain	SG-100CA
	Invert, Axial Strain	SG-100IA
	East, Axial Strain	SG-100EA
	West, Axial Strain	SG-100WA
75 in. South of FL	Crown, Axial Strain	SG-75CA
	Invert, Axial Strain	SG-75IA
	East, Axial Strain	SG-75EA
	West, Axial Strain	SG-75WA
50 in. South of FL	Crown, Axial Strain	SG-50CA
	Invert, Axial Strain	SG-50IA
	East, Axial Strain	SG-50EA
	East, Circumferential Strain	SG-50EC
	West, Axial Strain	SG-50WA
	West, Circumferential Strain	SG-50WC

Table 6.1 IPEX split basin strain gage instrumentation list (continued)

Location	Instrument Description	Local Instrument Name
25 in. South of FL	Crown, Axial Strain	SG-25CA
	Invert, Axial Strain	SG-25IA
	East, Axial Strain	SG-25EA
	East, Circumferential Strain	SG-25EC
	West, Axial Strain	SG-25WA
	West, Circumferential Strain	SG-25WC
At FL	Crown, Axial Strain	SG0CA
	Crown, Circumferential Strain	SG0CC
	Invert, Axial Strain	SG0IA
	Invert, Circumferential Strain	SG0IC
	East, Axial Strain	SG0EA
	East, Circumferential Strain	SG0EC
	West, Axial Strain	SG0WA
	West, Circumferential Strain	SG0WC
25 in. North of FL	Crown, Axial Strain	SG+25CA
	Invert, Axial Strain	SG+25IA
	East, Axial Strain	SG+25EA
	East, Circumferential Strain	SG+25EC
	West, Axial Strain	SG+25WA
	West, Circumferential Strain	SG+25WC
50 in. North of FL	Crown, Axial Strain	SG+50CA
	Invert, Axial Strain	SG+50IA
	East, Axial Strain	SG+50EA
	East, Circumferential Strain	SG+50EC
	West, Axial Strain	SG+50WA
	West, Circumferential Strain	SG+50WC
75 in. North of FL	Crown, Axial Strain	SG+75CA
	Invert, Axial Strain	SG+75IA
	East, Axial Strain	SG+75EA
	West, Axial Strain	SG+75WA
100 in. North of FL	Crown, Axial Strain	SG+100CA
	Invert, Axial Strain	SG+100IA
	East, Axial Strain	SG+100EA
	West, Axial Strain	SG+100WA

Table 6.1 IPEX split basin strain gage instrumentation list (continued)

Location	Instrument Description	Local Instrument Name
106 in. North of FL	Crown, Axial Strain	SG+106CA
	Crown, Circumferential Strain	SG+106CC
	Invert, Axial Strain	SG+106IA
	Invert, Circumferential Strain	SG+106IC
	East, Axial Strain	SG+106EA
	East, Circumferential Strain	SG+106EC
	West, Axial Strain	SG+106WA
	West, Circumferential Strain	SG+106WC
135 in. North of FL	Crown, Axial Strain	SG+135CA
	Invert, Axial Strain	SG+135IA
	East, Axial Strain	SG+135EA
	West, Axial Strain	SG+135WA
141 in. North of FL	Crown, Axial Strain	SG+141CA
	Invert, Axial Strain	SG+141IA
	East, Axial Strain	SG+141EA
	West, Axial Strain	SG+141WA
230 in. North of FL	East, Axial Strain	SG+230EA
	West, Axial Strain	SG+230WA

Table 6.2. Instrumentation for IPEX split basin test

End	Side	Instrument Description	Local Instrument Name
South	SE	Load Cell	LC3-6in-1K
	SW	Load Cell	LC5-6in-1K
	NE	Load Cell	LC6-6in-1K
	NW	Load Cell	LC7-6in-1K
		Pressure Sensor	Pressure Sensor 1
North	NE	Load Cell	LC8-6in-1K
	NW	Load Cell	LC10-6in-1K
	SE	Load Cell	LC11-6in-1K
	SW	Load Cell	LC12-6in-1K
		Pressure Sensor	Pressure Sensor 2

Table 6.3. Displacement instruments for IPEX split basin test

Location	Instrument Description	Instrument Name
South Joint Crown	String Pot	SP_S_CROWN
SE Joint 120 in.	String Pot	SP_SE
SW Joint 120 in.	String Pot	SP_SW
North Joint Crown	String Pot	SP_N_CROWN
NE Joint 120 in.	String Pot	SP_NE
NW Joint 120 in.	String Pot	SP_NW
North Slip	String Pot	SP_NS
South Slip	String Pot	SP_SS
East Fault	East Fault Displacement	DISP_E_FAULT
West Fault	West Fault Displacement	DISP_W_FAULT



(a)



(b)

Figure 6.2. Joint instrumentation (a) before and (b) after installation of joint shield

6.1.3. Soil Preparation and Compaction Data

The soil used during the IPEX large-scale fault rupture test was a crushed, washed, glacio-fluvial sand produced by RMS Gravel, the same as that described in Section 5.2. Figure 5.2 provides a grain size distribution of the RMS graded sand. The target value of dry density was $\gamma_{dry} = 106 \text{ lb/ft}^3$ (16.7 kN/m^3), and the target value of moisture content was $w = 4.0\%$, corresponding to an angle of shearing resistance (friction angle) for the sand of approximately 42° .

Eight measurements of dry unit weight and moisture content were made for each soil lift. Figure 6.3 shows the approximate location of each measurement location. There were four measurement

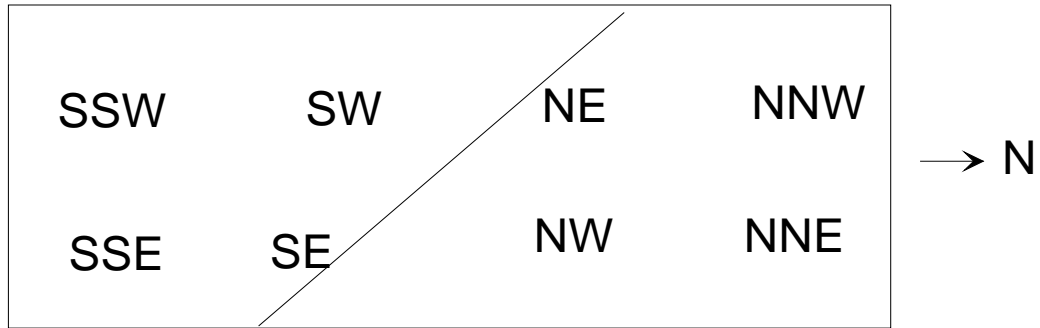


Figure 6.3. Plan view of locations for compaction measurements

positions in the north portion of the test basin and four in the south section for each soil lift. Table 6.4 lists the dry unit weights, and Table 6.5 provides the moisture contents. The global average dry unit weight was 106.4 lb/ft^3 (16.7 kN/m^3) with a standard deviation of 2.1 lb/ft^3 (0.3 kN/m^3). The global average moisture content was 4.2% with a standard deviation of 0.8%.

Table 6.4. Dry unit weights for IPEX pressurized pipe test

	Dry Unit Weights (lb/ft^3) ^a				
Location	Lift 1	Lift 2	Lift 3	Lift 4	Lift 5
NNW	103.0	104.0	106.8	109.4	105.8
NW	106.7	105.1	107.7	111.2	104.8
SSW	106.5	107.5	107.6	108.8	105.8
SW	104.5	107.8	109.5	108.5	104.2
SE	106.4	107.0	109.0	106.0	105.2
SSE	107.7	107.4	108.1	108.5	103.3
NE	106.7	106.5	106.4	104.8	103.7
NNE	104.0	107.2	107.4	100.0	105.0
Average	105.7	106.6	107.8	107.1	104.7
Stdev	1.6	1.3	1.0	3.5	0.9
Global Average					106.4
Global Stdev					2.1

$$1 \text{ (lb/ft}^3\text{)} = 0.1571 \text{ kN/m}^3$$

Table 6.5. Moisture tin water content data for IPEX pressurized pipe test

	Moisture Tin Water Content, w (%)				
Location	Lift 1	Lift 2	Lift 3	Lift 4	Lift 5
NNW	4.9	3.9	4.0	3.8	5.6
NW	4.9	3.7	4.2	3.0	6.2
SSW	4.0	3.5	3.8	3.8	4.2
SW	4.8	3.6	3.5	3.5	4.3
SE	3.8	4.9	4.7	3.3	4.3
SSE	4.4	3.6	5.4	4.4	4.8
NE	2.7	4.5	5.5	4.0	3.8
NNE	3.4	4.7	4.9	4.1	3.3
Average	4.12	4.04	4.51	3.73	4.57
Stdev	0.78	0.57	0.75	0.43	0.95
Global Average					4.2
Global Stdev.					0.8

6.2. Split Basin Test Results

Measurements obtained during the fault rupture test are summarized and described under the subheadings that follow.

6.2.1. Test Basin Movements

Four actuators are connected between the movable portion of the test basin and the modular reaction wall in the laboratory. From south to north, the actuators are identified as short-stroke actuator 1 (SSA1), short-stroke actuator 2 (SSA2), long-stroke actuator 1 (LSA1), and long-stroke actuator 2 (LSA2). Each SSA actuator has a displacement range of ± 2 ft (± 0.61 m) for a total stroke of 4 ft (1.22 m) and load capacity of 100 kips (445 kN) in tension and 145 kips (645 kN) in compression. Each LSA actuator has a displacement range of ± 3 ft (0.91 m) for a total stroke of 6 ft (1.83 m) and load capacity of 63 kips (280 kN) in tension and 110 kips (489 kN) in compression. The test configuration allows the actuators to displace the north half of the test basin a maximum of 43.5 in. (1.1 m).

Figure 6.4 shows the displacement of the four actuators, the average of which is the fault displacement, with respect to time. Since the servo controlled actuators move in unison under displacement control, all recorded displacements are identical.

Figure 6.5 shows the compressive load versus time for each actuator. As the northern part of the basin was moved toward the northwest, the tensile force and offset in the pipeline generated a moment to rotate the northern part of the basin in a counterclockwise direction. To maintain moment equilibrium, the actuators needed to generate an equal and opposite moment, which resulted in the largest compressive load being developed by the actuator closest to the fault, with a steady reduction in compressive force in each actuator north of the fault. A small tensile force was developed in the northernmost actuator to assist in maintaining basin alignment.

6.2.2. Internal Water Pressure

Figure 6.6 shows the pipe internal pressure versus fault displacement. The pipe was initially pressurized to 83 psi (572 kPa) before basin movement. Movement of the split basin caused the pipeline to increase in overall length, which resulted in moderate fluctuations in pressure between approximately 80 psi (552 kPa) and 85 psi (586 kPa). Pressure loss occurred at a fault displacement of 18.0 in. (457 mm) corresponding to rupture of the test specimen at the south side of the north joint.

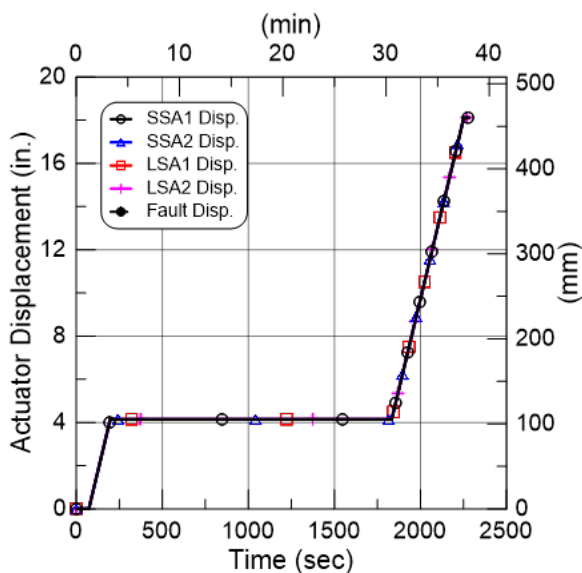


Figure 6.4. Actuator Displacement vs. Time

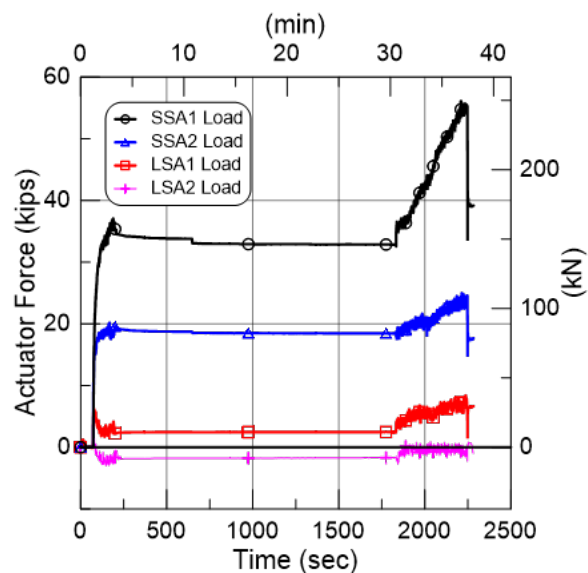


Figure 6.5. Actuator Force vs. Time

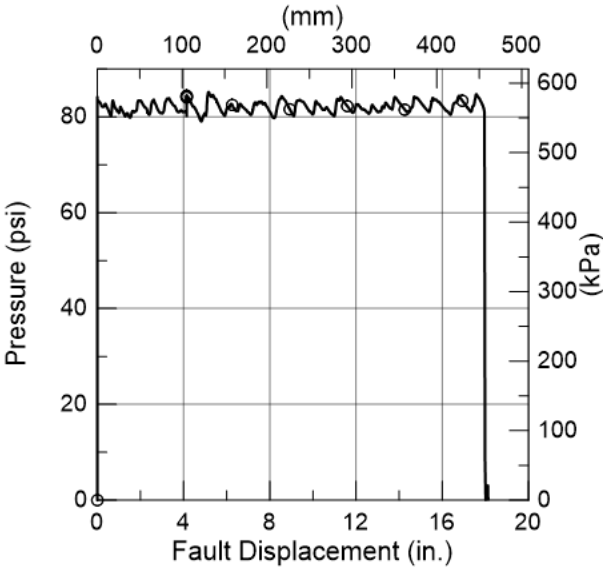


Figure 6.6. Internal water pressure vs. fault displacement

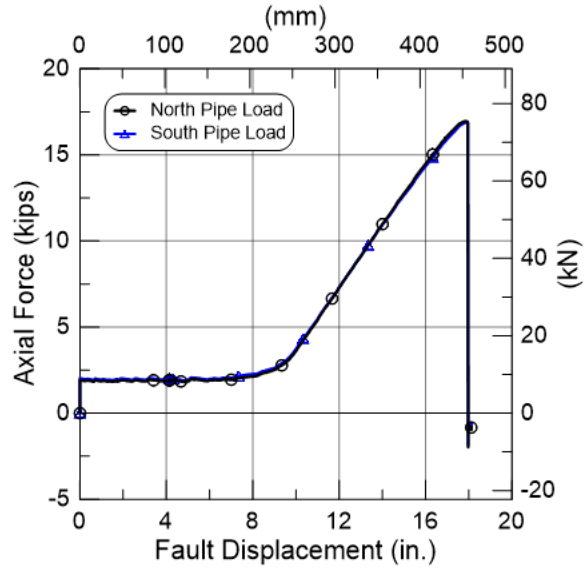


Figure 6.7. Measured north and south end axial force

6.2.3. End Loads

The axial end loads were measured with two exterior and two interior load cells at both the north and south ends of the test basin. The sum of the two exterior load cells at each end of the test basin gives the total axial end load. Figure 6.7 shows the total loads at the north and south ends of the test basin versus fault displacement. There is excellent agreement between them as expected, given the symmetry of this test.

An initial tensile end load of approximately 3 kips (13.3 kN) was present at the beginning of the test due to internal pressurization. This pressurization force was contained at the basin walls and did not impose loading to the buried section of the test specimen. At approximately 8 in. (203.2 mm) of fault displacement, there was full extension of the north and south joints after which the end loads increase rapidly. Load cell measurements recorded a peak force of 17 kips (75.6 kN) at 18 in. (457 mm) of fault displacement.

6.2.4. Joint Opening

A photo of the instrumented joint prior to burial is provided in Figure 6.2, and a drawing of the initial joint configuration is provided in Figure 6.8. The joint opening recorded by three string potentiometers located within shields at the south and north joints is shown in Figure 6.9. Excellent

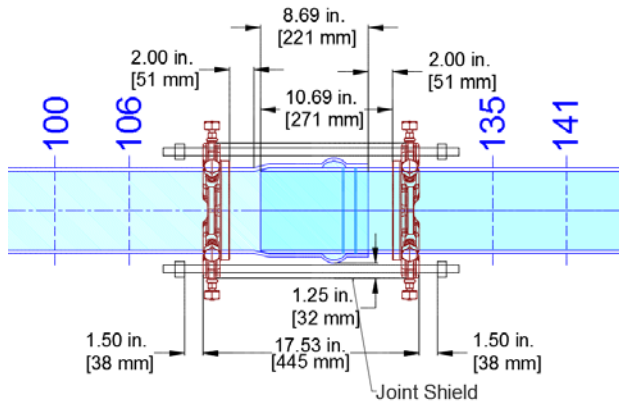


Figure 6.8. Initial conditions of restrained joint

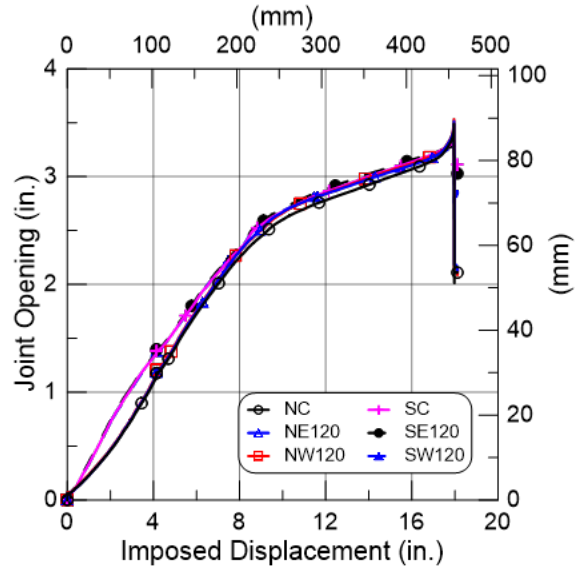


Figure 6.9. Joint opening displacement for both joints relative to fault displacement

agreement among all three string pots at each joint is shown in the figure, indicating little joint rotation during fault rupture. The south joint opens slightly sooner than the north joint, but for the most part the response is symmetrical. At about 8 in. (200 mm) of fault rupture, corresponding to 2.5 in. (64 mm) of joint opening, the nearly linear joint opening response changes, with greater fault displacement corresponding to equivalent increases in joint opening. Significant axial resistance was initiated at 2.5 in. (64 mm) of joint opening even though the nuts were set to allow 3.0 in. (76 mm) of axial movement before contact with the restraining collars. The reduced 2.5 in. (64 mm) of joint opening may be due to soil becoming wedged between the restraining nuts and collar, as described previously for the axial pull tests. The maximum joint opening was approximately 3.5 in. (89 mm).

6.2.5. Axial Strain and Force Distribution

The average axial strains at each gage plane along the pipeline are shown in Figure 6.10 for various levels of fault displacement. As described previously, the joints were located 120.5 in. (3.06 m) from the fault rupture plane on either side of the fault crossing, as indicated in the figure.

Figure 6.10 shows relatively small compressive strains at some gage planes before fault movement. These strains result from Poisson's effect whereby internal pressurization causes contraction of

the pipe in the longitudinal direction as it slips at the joints. Axial strains are relatively small during the first 6 in. (150 mm) of fault displacement, before engagement of the joints. After approximately 8 in. (200 mm) of fault movement strains begin to increase more rapidly along the entire pipe length, including the sections of pipe north and south of the north and south joints, respectively. The axial tensile strains increase along the pipeline with increased fault displacement. Drops in strain are apparent across each of the restrained joints, demonstrating the increased axial force required to develop relative displacement between restraint and soil.

The axial strains at the largest increment of fault displacement [17.96 in. (456.2 mm)] correspond to the maximum axial load before failure of the pipeline. Axial strains at gage planes closest to the end of the test basin (SG±230) reach maximum values of 0.85% and 0.8%, respectively. Maximum axial strains of 1.42 to 1.48% were measured at gage planes SG±25 located on either side of the fault crossing just before failure. These symmetric peaks were likely influenced by bending that developed in the pipe at these locations (see the following section for bending strains).

The outside diameter of the pipe was OD = 6.9 in. (175.3 mm) and the average measured wall thickness was $t_w = 0.245$ in. (6.22 mm). This gives a pipe wall cross-sectional area of $A = 5.12$ in.² (3305 mm²). As previously reported, the average Young's modulus of the Bionax PVC0 in the elastic range was $E = 450$ ksi (3.10 GPa) and the variation of secant modulus with axial strain is provided in Figure 5.3. Using the average axial strain at each plane and multiplying the strain times AE provides an estimate of the axial force in the pipe.

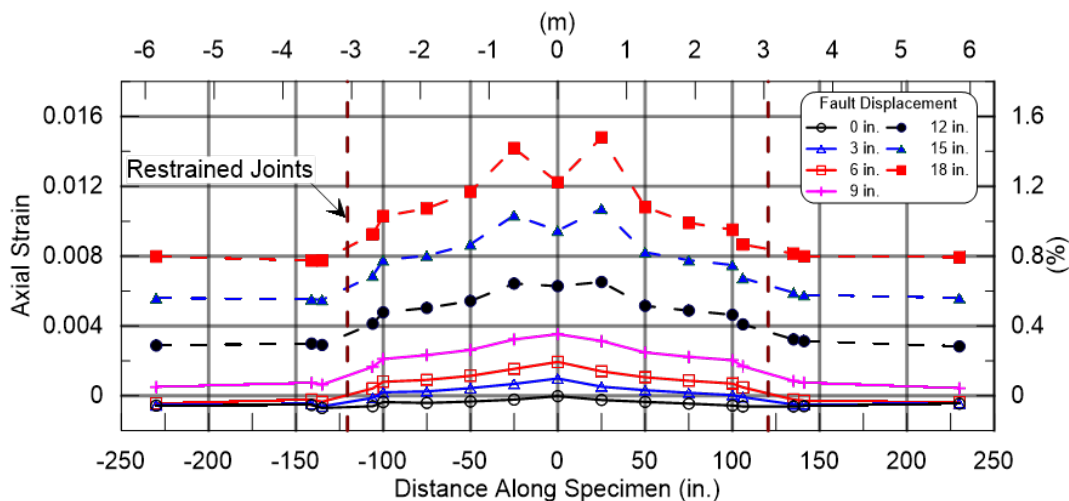


Figure 6.10. Evolution of average axial strains along pipeline at various magnitudes of fault movement

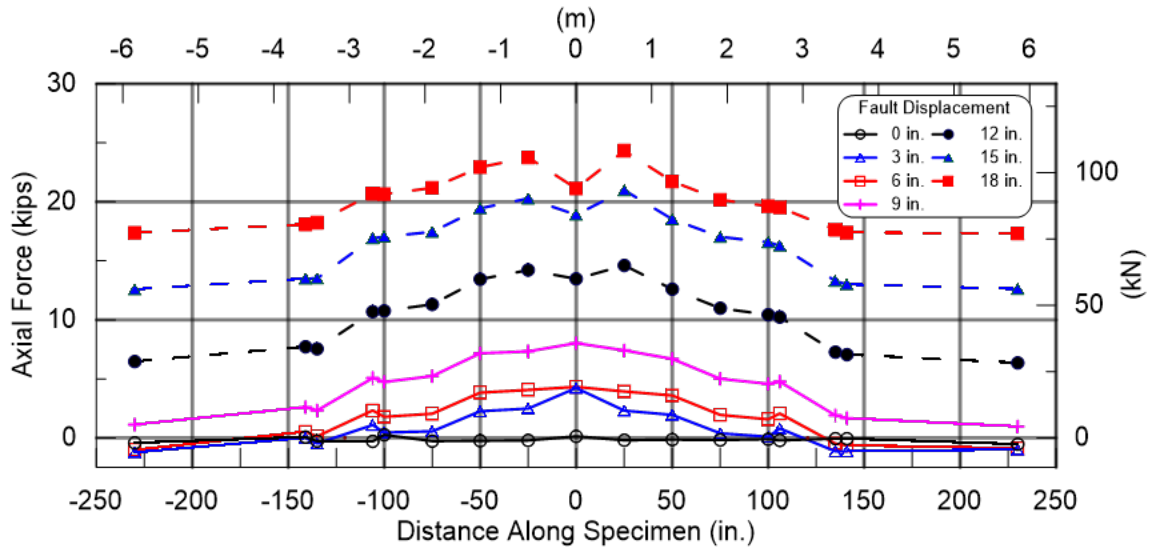


Figure 6.11. Evolution of average axial force along pipeline at various magnitudes of fault movement

The distribution of axial force along the pipe, again calculated as axial force, $F = \epsilon AE$, is shown in Figure 6.11. There is a steady accumulation of axial force as fault displacement increases, with the maximum force of 24.3 kips (108 kN) at SG+25 located 25 in. (635 mm) north of the fault crossing. The maximum axial force at the fault crossing (0 distance) was 21.1 kips (94 kN). The axial force distribution follows similar trends as the axial strain along the pipe.

6.2.6. Bending Strain and Moment Distribution

The bending strain, ϵ_b , is calculated as:

$$\epsilon_b = \frac{\epsilon_W - \epsilon_E}{2} \quad (6.1)$$

Where ϵ_E is the measured strain at the gage mounted in the axial direction on the east springline and ϵ_W is the measured strain at the gage mounted in the axial direction on the west springline.

When using this sign convention the direct axial strain on the east side is $\epsilon_{AE} = \epsilon_E + \epsilon_b$, and the direct axial strain on the west side is $\epsilon_{AW} = \epsilon_W - \epsilon_b$.

Figure 6.12 presents the bending strains along the pipeline for various levels of fault displacement, demonstrating an anti-symmetric pattern of strain centered on the fault. The locations of the joints

are shown at distances 120.5 in. (3.06 m) north and south of the rupture plane. Bending strains north and south of the joints were very low throughout the test.

Figure 6.12 shows that, during the first 9 in. (229 mm) of fault displacement, there were relatively large increases in bending strains, after which the joints fully extend and axial tension dominates specimen response. The largest strains were measured at planes SG+25 (-1.4%) and SG-25 (1.23%), located on either side of the rupture plane.

The experimental bending strain, ϵ_b , was converted to bending moment, M , through the expression:

$$M = \frac{2EI\epsilon_b}{D} \quad (6.2)$$

where E is the Young's modulus for a particular strain level, I is the pipe moment of inertia, ϵ_b is the bending strain, and D is the pipe outer diameter.

Figure 6.13 presents the bending moment distribution along the pipeline in a manner similar to that used for Figure 6.12. As expected, the bending moments follow closely the distribution of bending strains. For higher fault displacements, the imposed strains caused the pipe stresses to exceed the proportional limit, resulting in a lower nonlinear pipe stiffness used in Equation 4.3 when calculating pipe stresses from pipe strains.

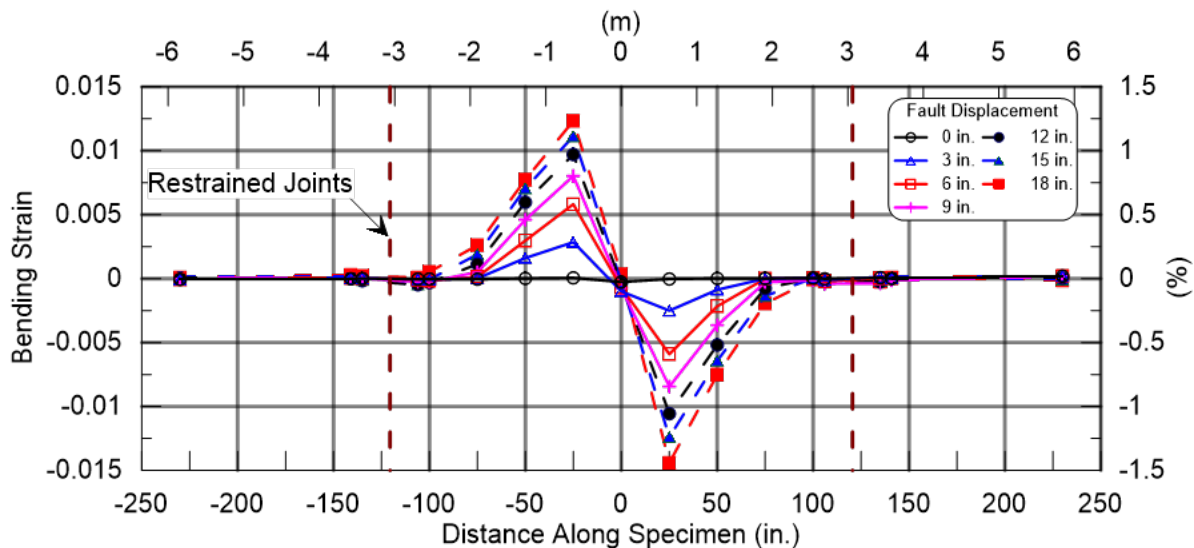


Figure 6.12. Evolution of bending strains along the specimen at various levels of fault rupture

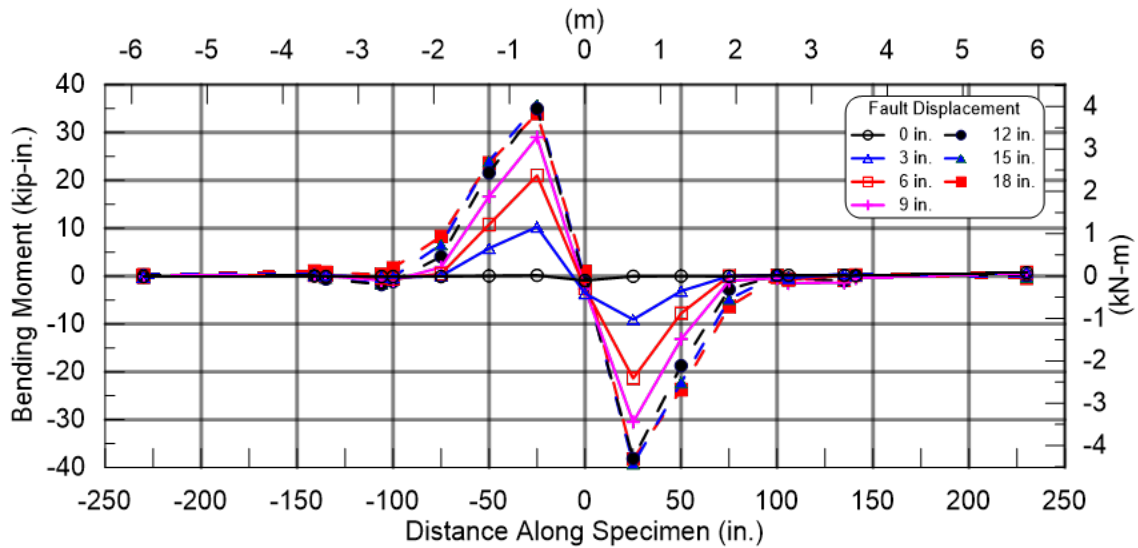


Figure 6.13. Evolution of bending moment along pipeline at various magnitudes of fault movement

6.3. Post-test Photos

This section includes photos of the pipeline after excavation at the end of the test to expose and examine the pipe. Figure 6.14 shows an overhead photo of the pipe and a close-up photo of the failed joint after excavation. North is to the right in both images. Figure 6.15 shows photos looking north of the specimen after excavation. Figure 6.15(b) provides a close-up view of the failed specimen and circumferential fracture.

6.4. Summary of Split Basin Test

A 40.4 ft (12.3 m) long 6-in. (150-mm)-diameter Bionax SR PVCO pipeline with two restrained joints positioned 10 ft (3.1 m) on either side of a 50 degree fault rupture plane was tested at the Cornell Large-Scale Testing Facility. The pipe was instrumented with eighty-eight strain gages installed at nineteen locations along the pipeline to measure axial and circumferential strains and to evaluate axial forces and bending moments. Strain gages were positioned at the crown (C), invert (I) east (E) springline, and west (W) springline of the pipe. Three string pots were used at each joint to measure pullout displacement and rotation. Four load cells were placed at each end of the specimen, reacting between the test basin structural frame and pipe end restraints to measure axial force. The pipe was pressurized to approximately 80 psi (552 kPa) throughout the test.

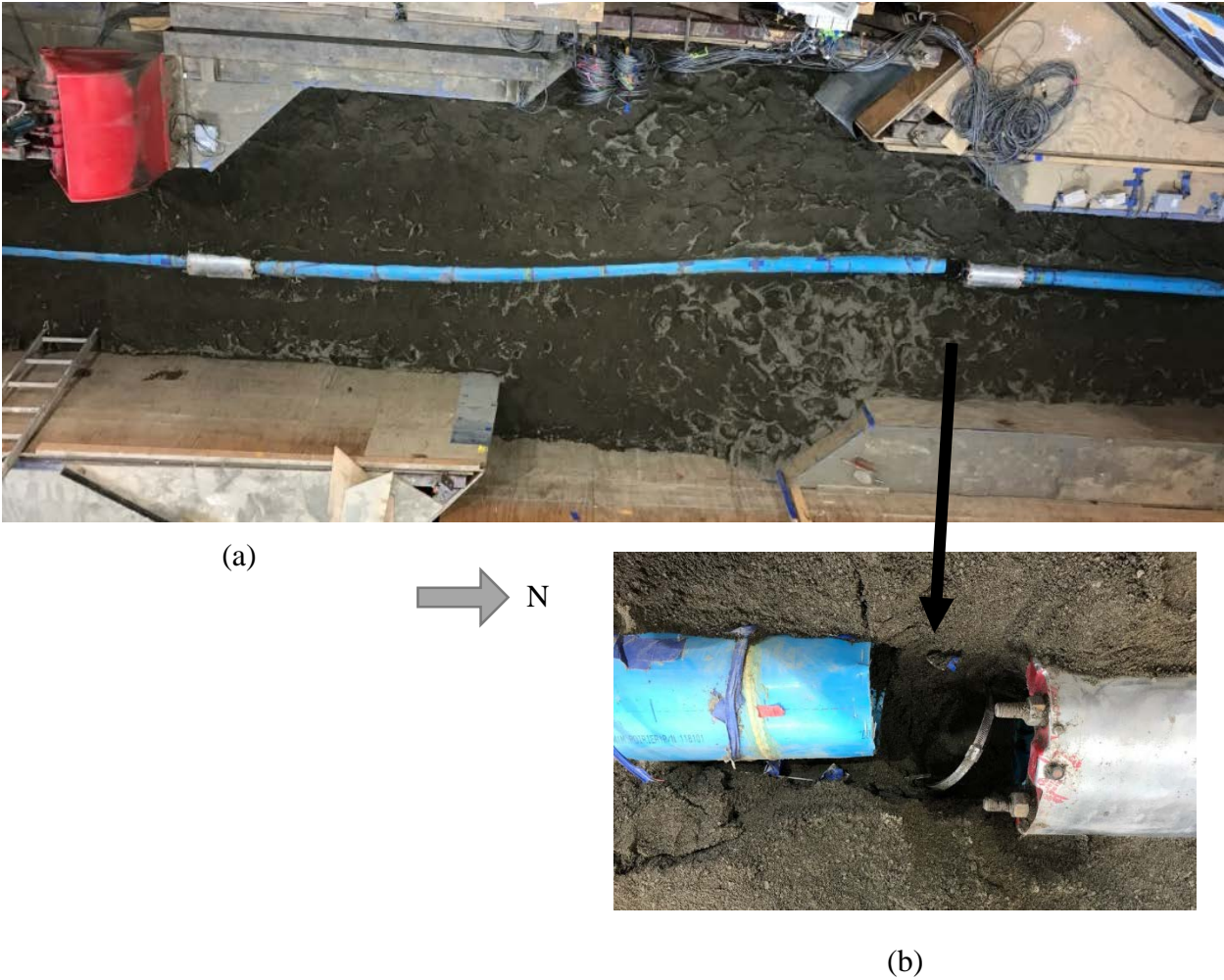
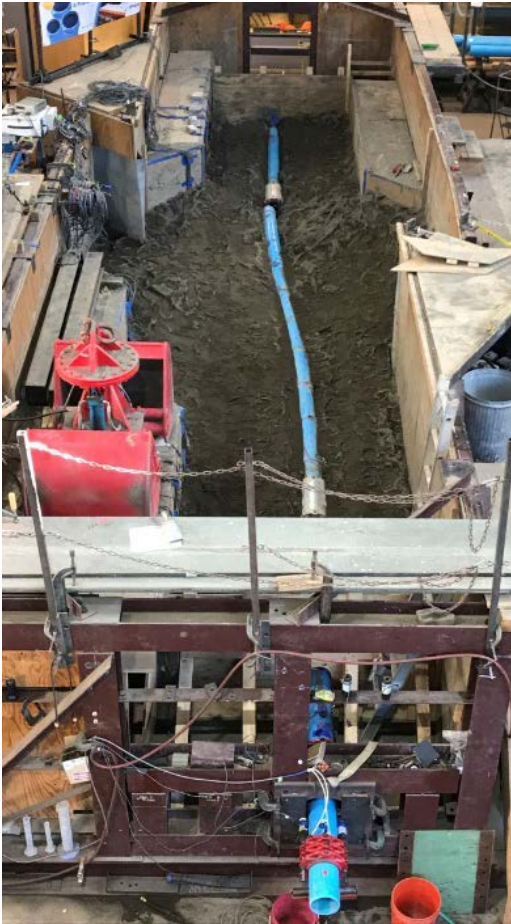


Figure 6.14. Overhead view of the (a) pipeline and (b) failed joint after excavation of the split basin test

The pipeline was buried in the Cornell large-scale test basin in partially saturated sand that was compacted to have an average friction angle of 42° , equivalent in strength to that of a medium dense to dense granular backfill. The 6.9-in. (175-mm) outer-diameter pipe was placed on a bed of soil with 13-in. (330-mm) thickness at the bottom of the test basin and soil was placed in lifts until the depth of burial to top of pipe was 32 in. (800 mm). During the test, the south part of the basin remained stationary, while the north part was displaced to the north and west by large-stroke actuators to cause soil rupture and slip at the interface between the two parts of the test basin.

The north section of the test basin was displaced along a 50° fault at a rate of 2 in. (50 mm) per minute. The basin was displaced 4 in. (100 mm), followed by a pause and an additional 14 in.



(a)



(b)

Figure 6.15. View looking north of (a) failed pipeline and (b) close up of joint

(350 mm) of movement along the fault. At 18.0 in. (457 mm) of total fault movement pressure loss occurred, corresponding to rupture of the test specimen at the south side of the north joint. This fault offset corresponds to 11.6 in. (294 mm) of axial tension of the basin and pipe.

The test measurements confirm that the pipeline was able to accommodate substantial fault movement through joint opening, development of axial strain along the pipe barrel, and bending of the pipe prior to leakage or rupture. The test also confirms the performance of the joint when the joint restraint system is set to 3.0 in. (76 mm) of allowable opening.

In addition to the Cornell instrumentation, additional measurements were collected with special sensors through collaboration with researchers at the University of California at Berkeley and the University of Cambridge Center for Smart Infrastructure and Construction. These special sensors

included (1) distributed fiber optic sensors to measure continuous strain along the pipe, (2) fiber Bragg grating sensors to measure strain along the specimen and displacement at the springlines of each joint, and (3) an array of moisture sensors (leakage detection) which transmitted data through the soil using a coupled magnetic induction and electromagnetic wireless sensor network. There was favorable comparison between the measurements reported in this section and the data obtained with the special sensors, thereby validating the sensors systems at field scale under conditions of extreme ground deformation. Additional information about the special sensor measurements will be available in supplementary publications.

Section 7

Summary

This report presents the test results from a program to investigate the performance of nominal 6-in. (150-mm)-diameter Bionax SR PVC pipe under significant levels of deformation such as those associated with ground rupture. The testing program reported herein is the second series performed at Cornell University on IPEX Bionax PVC pipe. A summary of material characterization previously conducted (Stewart et al., 2013a and Wham et al., 2017) is provided along with a description of the two joint restraints used during the testing program is discussed.

7.1. Tension Test Summary

Two tension tests are reported using two different joint restraints. The intention of testing both restraints was to determine which was best suited for developing axial force and strain along the pipeline during ground movement. These test results show that the Ford Meter Box 1559 restraints for a pressurized pipe provide 40% more load capacity compared to the Ford Meter Box 1309 restraints, and thus are able to mobilize approximately 40% more axial elongation in the pipe compared to the elongation that accompanies the maximum load before slippage with the black 1309 restraints. However, the slippage associated with the 1309 restraints results in greater axial displacement of the joint relative to that attained with the 1559 restraints. The 1559 restraints result in more elongation, or stretch, in the pipe between joints, whereas the 1309 restraints result in more slip at the individual joints with less pipe elongation.

7.2. Compression Test Summary

A compression test was performed on a 124 in. (3.1 m) long section Bionax SR pipe with the bell and spigot joint centered between two 1559 restraints. The pipe was pressurized with approximately 80 psi (550 kPa) of water throughout the test. An initial actuator displacement of 8 in. (200 mm) was applied to the pipe section, followed by several additional shorter loading sequences for a total 9.7 in. (296 mm) displacement at the joint. The joint sustained significant compressive deformation without leakage or loss of internal pressure. The spigot was pushed 6.5 in. (165 mm) and 5.1 in. (130 mm) past the end of the bell and bell collar location, respectively, demonstrating the capacity of the Bionax pipe with extended bell to accommodate axial compression. The compressive force versus axial displacement relationship for this test is

consistent with the results of previous testing performed at Cornell University on Bionax bell and spigot joints (Stewart et al., 2013a).

7.3. Four-point Bending Test Summary

A four point bending test was performed on an 18 ft (5.5 m) long section of Bionax SR pipe with the restrained bell and spigot joint centered on the frame. Loading points were positioned 30 in. (0.76 m) on either side of center. The pipe was pressurized with approximately 80 psi (550 kPa) of water throughout the test. The first vertical displacement of 2.5 in. (64 mm) was due to the self-weight of the pipe when support jacks were removed. Initial loading was applied solely through the downward movement of the crosshead with a pause at 13.3 in. (338 mm) to survey the springline. After 18.5 in. (470 mm) of vertical displacement, the crosshead was locked and additional loading was applied using the 6 in. (152 mm) stroke MTS actuator until failure at a total vertical displacement of 24.3 in. (617 mm).

A maximum moment of 52 kip-in. (5.9 kN-m) occurred at a deflection of 43 degrees. There was a reduction in moment for the remainder of the test until failure at maximum rotation of 47.5 degrees. As shown by the photos and test measurements, the joint was able to sustain substantial deformation without leakage or loss of internal pressure before failure.

7.4. Axial Pull Tests Summary

Four axial pull tests were performed on restrained joints. Three tests were performed with the 1559 restraints at soil depths to crown of pipe of 30, 45, and 60 in. (760, 1140, and 1520 mm). The fourth test was conducted at a depth to top of pipe of 45 in. (1140 mm) with the 1309 restraints. During each test the pipe was pulled approximately 30 in. (760 mm) through the soil.

Axial force vs displacement plots are presented and compared for the four tests in which the actuator load and axial load measured at 21 in. (533 mm) north of the bell face are plotted with respect to the leading edge displacement. Combining the axial loads measured at 21 in. (533 mm) north of the bell face with the leading edge displacements is equivalent to plotting the load drops across the restrained joint versus relative axial displacement between the restrained joint and soil. The successively higher load drops at increasingly deeper burial depths are shown clearly in the plots. The magnitude of resistance changes with relative displacement, and increases linearly with soil depth. The size of the restraint also affects resistance with the smaller 1309 restraint

generating 20% less axial force to pull through the soil than that required to pull the 1559 restraints at identical burial depths in the same soil.

7.5. Summary of Large-Scale Fault Rupture Effects

A 40.4 ft (12.3 m) long 6-in. (150-mm)-diameter Bionax SR PVCO pipeline with two restrained joints positioned 10 ft (3.1 m) on either side of a 50 degree fault rupture plane was tested at the Cornell Large-Scale Testing Facility. The pipe was instrumented with eighty-eight strain gages installed at nineteen locations along the pipeline to measure axial and circumferential strains and to evaluate axial forces and bending moments. Strain gages were positioned at the crown (C), invert (I) east (E) springline, and west (W) springline of the pipe. Three string pots were used at each joint to measure pullout displacement and rotation. Four load cells were placed at each end of the specimen, reacting between the test basin structural frame and pipe end restraints to measure axial force. The pipe was pressurized to approximately 80 psi (552 kPa).

The pipeline was buried in the Cornell large-scale test basin in partially saturated sand that was compacted to have an average friction angle of 42° , equivalent in strength to that of a medium dense to dense granular backfill. The 6.9-in. (175-mm) outer-diameter pipe was placed on a bed of soil with 13-in. (330-mm) thickness at the bottom of the test basin and soil was placed in lifts until the depth of burial to top of pipe was 32 in. (800 mm). During the test, the south part of the basin remained stationary, while the north part was displaced to the north and west by large-stroke actuators to cause soil rupture and slip at the interface between the two parts of the test basin.

The north section of the test basin was displaced along a 50° fault at a rate of 2 in. (50 mm) per minute. The basin was displaced 4 in. (100 mm), followed by a pause and an additional 14 in. (350 mm) of movement along the fault. At 18.0 in. (457 mm) of total fault movement pressure loss occurred corresponding to rupture of the test specimen at the south side of the north joint. This fault offset corresponds to 11.6 in. (294 mm) of axial displacement of the basin and pipe.

The test measurements confirm that the pipeline was able to accommodate substantial fault movement through joint opening, development of axial strain along the pipe barrel, and bending of the pipe prior to leakage or rupture. The test also confirms the performance of the joint when the joint restraint system is set for 3.0 in. (76 mm) of allowable opening. Larger diameter Bionax

pipe has a deeper bell that provides for increased joint opening, thus allowing larger diameter pipelines to accommodate greater fault displacement.

The combined results of the large-scale fault rupture test and tension, compression, and four point bending tests demonstrate the capacity of Bionax SR PVCO pipe with Series 1559 Uni-Flange® Pipe Restraints to respond favorably to large ground deformation. During the fault rupture test, the combined axial pullout of the two joints of approximately 7 in. (178 mm) over the pipeline length of 496 in. (12600 mm) [from south end load cells to north end load cells] resulted in 1.4 % axial extension that adds to the 1% average tensile strain in the pipeline (see Figure 6.10) for a total 2.4% axial elongation of the pipeline. Pipe failure occurred when axial load carried by the restrained joint was 21 - 22 kips (93 – 98 kN). The four-point bending test results show a relative rotation of 47 degrees, which demonstrates substantial capacity to accommodate differential settlement and/or lateral displacement along the pipeline. The compression test confirmed pipeline capacity to accommodate large compressive movement by axial spigot slip as high as 6.5 in. (165 mm) past the end of the bell of a restrained joint into the adjacent straight pipe segment.

7.6. Significance of Test Results

Large-scale tests at Cornell demonstrate the ability of the Bionax SR PVCO pipe with restrained joints to accommodate significant fault movement through axial tension, bending, and compression of the joints and pipe barrel. Fault rupture simulated in the large-scale test is also representative of the most severe ground deformation that occurs along the margins of liquefaction-induced lateral spreads and landslides. A significant advantage of the deep bell Bionax SR PVCO pipe with restrained joints is the ability for the pipeline to adjust to ground deformation through axial slip at the joints combined with tensile elongation of the pipe between the joints.

The amount of ground movement that can be accommodated with the Bionax SR restrained joint pipeline system will depend on several factors, including the depth of burial and the number and spacing of joints relative to the location of abrupt ground movement. The pipeline used in the large-scale split-basin test was able to accommodate 11.6 in. (294 mm) of axial extension, corresponding to an average tensile strain of 2.4% along the pipeline. Such capacity is large enough to accommodate the great majority (approximately 97-98%) of liquefaction-induced ground strains measured by high resolution LiDAR after each of four major earthquakes during

the recent Canterbury Earthquake Sequence (CES) in Christchurch, NZ (Bouziou, et al., 2015; O'Rourke, et al., 2014). To put the CES ground strains in perspective, liquefaction-induced ground deformation measured in Christchurch exceed those documented in San Francisco during the 1989 Loma Prieta earthquake (e.g., O'Rourke and Pease, 1997; Pease and O'Rourke, 1997) and in the San Fernando Valley during the 1994 Northridge earthquake (e.g., O'Rourke, 1998). They are comparable to the levels of most severe liquefaction-induced ground deformation documented for the 1906 San Francisco earthquake, which caused extensive damage to the San Francisco water distribution system (e.g., O'Rourke and Pease, 1997; O'Rourke, et al., 2006).

References

- ASTM International (2013) “Standard Test Methods for Tension Testing of Metallic Materials”, *ASTM Standards*. E8/E8M - 13a, 1 – 28.
- Bouziou, D., T. D. O’Rourke, M. Cubrinovski, and D. Henderson (2015) “Evaluation of Ground Deformations during the 2010-2011 Canterbury Earthquake Sequence”, *Proceedings*, 6th Intl. Conf. on Earthquake Geotech. Engr., Christchurch, NZ, 8.
- Bower, A. F. (2010) *Applied Mechanics of Solids*, Boca Raton, Fla: CRC Press.
- Ford Meter Box Company (2017) “Pipe Restraints and Adapter Flanges for PVC, Ductile Iron and Steel Pipe,” Ford Meter Company, Wabash, IN, <http://www.fordmeterbox.com/catalog/u/ujpeg.pdf> , last accessed September 22, 2017.
- O’Rourke, T. D. (1998) “An Overview of Geotechnical and Lifeline Earthquake Engineering”, *Geotechnical Special Publication No. 75*, ASCE, Reston, VA, Proceedings of Geotechnical Earthquake Engineering and Soil Dynamics Conference, Seattle, WA, Aug. 1998, Vol. 2, pp.1392-1426.
- O’Rourke, T. D. and J. W. Pease (1997) “Mapping Liquefiable Layer Thickness for Seismic Hazard Assessment”, *Journal of Geotechnical Engineering*, ASCE, New York, NY, Vol. 123, No.1, January, pp. 46-56.
- O’Rourke, T. D., A. Bonneau, J. Pease, P. Shi, and Y. Wang (2006) “Liquefaction Ground Failures in San Francisco”, *Earthquake Spectra*, EERI, Oakland, CA, Special 1906 San Francisco Earthquake, Vol. 22, No. 52, Apr., pp. 691-6112.
- O’Rourke, T. D., Jeon, S-S., Toprak, S., Cubrinovski, M., Hughes, M., van Ballegooy, S., and Bouziou, D. (2014) “Earthquake Response of Underground Pipeline Networks in Christchurch, NZ”, *Earthquake Spectra*, EERI, Vol. 30, No.1, pp. 183-204.
- Pease, J. W. and T. D. O’Rourke (1997) “Seismic Response of Liquefaction Sites”, *Journal of Geotechnical Engineering*, ASCE, New York, NY, Vol. 123, No. 1, January, pp. 37-45.
- Sanchez, L. (2013) “Test Report on Over-insertion of 200 mm Bionax Joint”, IPEX Inc.: Internal Report. Saint-Laurent, QC, Canada.
- Stewart, H. E., Wham, B. P., O’Rourke, T. D., & Bond, T. K. (2013a), “Task 1 - Material Testing of Bionax Pipe and Joints”, Cornell University, Ithaca, NY, <https://lifelines.cee.cornell.edu/> , last accessed September 22, 2017.
- Stewart, H. E., Wham, B. P., O’Rourke, T. D., & Bond, T. K. (2013b). “Task 2 - Four-Point Bending of Bionax Pipe and Pipe Joints”, Cornell University, Ithaca, NY, <https://lifelines.cee.cornell.edu/> , last accessed September 22, 2017.

- Stewart, H. E., Wham, B. P., O'Rourke, T. D., Bouziou, D., Argyrou, C., & Bond, T. K. (2013c) "Task 3 - Large-Scale Testing of Fault Rupture Effects on Bionax Pipe and Pipe Joints", Cornell University, Ithaca, NY, <https://lifelines.cee.cornell.edu/> , last accessed September, 22, 2017.
- Wham, B. P., Argyrou, C., O'Rourke, T. D., Stewart, H. E., & Bond, T. K. (2017) "PVCO Pipeline Performance Under Large Ground Deformation", J. of Pressure Vessel Technology, ASME. Vol.139(1). doi:10.1115/1.4033939.
- Wham, B. P., Argyrou, C., O'Rourke, T. D., Stewart, H. E., and Bond, T. K. (2015) "PVCO Pipeline Performance Under Large Ground Deformation", *Proceedings*, International Pipeline Geotechnical Conference, Bogota, Columbia, Paper ID: 8508.
- Wham, B.P. (2016). "Jointed Pipeline Response to Large Ground Movement", Ph.D. Thesis, Cornell University, Ithaca, NY.